



A modified error in constitutive equation approach for frequency-domain viscoelasticity imaging using interior data

Manuel I. Diaz, Wilkins Aquino, Marc Bonnet

► To cite this version:

Manuel I. Diaz, Wilkins Aquino, Marc Bonnet. A modified error in constitutive equation approach for frequency-domain viscoelasticity imaging using interior data. *Computer Methods in Applied Mechanics and Engineering*, 2015, 296, pp.129-149. 10.1016/j.cma.2015.07.025 . hal-01183511

HAL Id: hal-01183511

<https://hal.science/hal-01183511>

Submitted on 11 Aug 2015

HAL is a multi-disciplinary open access archive for the deposit and dissemination of scientific research documents, whether they are published or not. The documents may come from teaching and research institutions in France or abroad, or from public or private research centers.

L'archive ouverte pluridisciplinaire **HAL**, est destinée au dépôt et à la diffusion de documents scientifiques de niveau recherche, publiés ou non, émanant des établissements d'enseignement et de recherche français ou étrangers, des laboratoires publics ou privés.

A Modified Error in Constitutive Equation Approach for Frequency-Domain Viscoelasticity Imaging Using Interior Data

Manuel I. Diaz^a, Wilkins Aquino^{a,*}, Marc Bonnet^b

^a*Department of Civil and Environmental Engineering, Duke University, Durham, North Carolina 27708 USA*

^b*POems (UMR 7231 CNRS-ENSTA-INRIA), Dept. of Appl. Math., ENSTA, Paris, France*

Abstract

This paper presents a methodology for the inverse identification of linearly viscoelastic material parameters in the context of steady-state dynamics using interior data. The inverse problem of viscoelasticity imaging is solved by minimizing a modified error in constitutive equation (MECE) functional, subject to the conservation of linear momentum. The treatment is applicable to configurations where boundary conditions may be partially or completely underspecified. The MECE functional measures the discrepancy in the constitutive equations that connect kinematically admissible strains and dynamically admissible stresses, and also incorporates the measurement data in a quadratic penalty term. Regularization of the problem is achieved through a penalty parameter in combination with the discrepancy principle due to Morozov. Numerical results demonstrate the robust performance of the method in situations where the available measurement data is incomplete and corrupted by noise of varying levels.

1. Introduction

Inverse characterization of viscoelastic properties is of high relevance in many areas of science, engineering, and medicine. In particular, in the medical field, it is well-known that viscoelastic properties are correlated to tissue pathology [28]. This observation has spurred the development of a group of techniques, commonly referred to as elastography or elasticity imaging techniques, whose goal is to identify the elastic or viscoelastic properties of tissue non-invasively (see [13, 24, 22, 15, 25] for reviews). Other applications abound and include the nondestructive evaluation of structural systems such as buildings, bridges, and aircraft components.

In this work, we are concerned with the quantification of viscoelastic material properties using noisy interior data, in situations where traction and/or displacement boundary conditions are unknown or uncertain. This problem is of high relevance in the field of elasticity imaging where displacement or velocity fields are obtained using ultrasound or MRI, and there is a high degree of uncertainty regarding the magnitude and nature of the excitation sources. Different techniques have been developed that address this problem, including algebraic direct inversion [21, 28, 23] and the adjoint weighted equations (AWE) methods [2, 30]. These techniques have the advantage of being non-iterative but need the evaluation of derivatives of the data, making them very sensitive to noise. Moreover, optimization approaches [10, 20, 11, 7, 1], which have the advantage of handling sparse and imperfect data, have received limited or no attention for problems with interior data that lack knowledge of the boundary conditions due to the complication of the forward problem then being ill-posed.

Our goal in this work is to develop a methodology for reconstructing viscoelastic properties from imperfect interior data and underspecified boundary conditions. The proposed methodology is based on the minimization of a *modified error in constitutive equation* (MECE) functional [18, 11, 4]. MECE functionals

*Corresponding author: Tel: +1 919 684 1922

Email addresses: manuel.diaz@duke.edu (Manuel I. Diaz), wa20@duke.edu (Wilkins Aquino), mbonnet@ensta.fr (Marc Bonnet)

combine the error in constitutive equation (ECE) [17], which measures the discrepancy in the constitutive equations that connect kinematically admissible strains and dynamically admissible stresses, and a quadratic error term that incorporates the measurement data. MECE-based approaches have found applications in model updating with vibrational data [18, 5], time-domain formulations [3, 11], and large scale identification problems in both elastodynamics [4] and coupled acoustic-structure systems [29]. MECE-based identification methods investigated thus far assume situations where well-posed boundary conditions are available. By contrast, one of the main features of the present approach is the fact that the proposed MECE formulation leads to optimality systems that are invertible, subject to a solvability condition that is easily met in practice, even in cases where (i) boundary conditions are (totally or partially) underspecified, and (ii) interior data is available only in a portion of the solid under investigation. This result is moreover achieved by exploiting classical first-order optimality conditions only. Some of the limitations inherent to other optimization-based formulations are therefore avoided. In addition, we adapt previous ideas regarding the solution strategy for the minimization problem to the realms of viscoelasticity, where positivity requirements are enforced using inequality constraints.

The rest of this article is organized as follows. Section 2 describes the steady-state viscoelasticity problem and the inverse problem of interest. The MECE-based minimization strategy is derived in Section 3, which also addresses the adjustment of its main parameters. Section 4 is devoted to a set of numerical experiments designed to demonstrate the capabilities of the method. Concluding remarks are finally given in Section 5.

2. Problem Setting

Governing equations of motion. Let a solid viscoelastic body occupy a bounded and connected domain $\Omega \subset \mathbb{R}^d$ ($1 \leq d \leq 3$) with boundary Γ . The time-harmonic motion of this body is governed by the balance equations

$$\nabla \cdot \boldsymbol{\sigma} + \mathbf{b} = -\rho\omega^2 \mathbf{u} \quad \text{in } \Omega, \quad (1a)$$

$$\boldsymbol{\sigma} \cdot \mathbf{n} = \mathbf{t} \quad \text{on } \Gamma_N, \quad (1b)$$

where \mathbf{u} is the displacement field, ω represents the specified angular frequency, ρ denotes the known mass density, \mathbf{b} is a given body force density, $\boldsymbol{\sigma}$ represents the stress tensor, \mathbf{t} and $\Gamma_N \subseteq \Gamma$ are the given surface force density (traction) and its support, respectively, and \mathbf{n}_s is the outward unit vector normal to Γ ; the kinematic compatibility equations

$$\mathbf{u} = \mathbf{0} \quad \text{on } \Gamma_D, \quad (2a)$$

$$\boldsymbol{\epsilon}[\mathbf{u}] = \frac{1}{2}(\nabla \mathbf{u} + \nabla \mathbf{u}^T) \quad \text{in } \Omega, \quad (2b)$$

where $\boldsymbol{\epsilon}[\mathbf{u}]$ denotes the linearized strain tensor associated with \mathbf{u} and $\Gamma_D \subseteq \Gamma$ is the portion of the boundary where the displacement is known; and the (linear viscoelastic) constitutive relation

$$\boldsymbol{\sigma} = \boldsymbol{\mathcal{C}} : \boldsymbol{\epsilon}[\mathbf{u}] \quad \text{in } \Omega, \quad (3)$$

where $\boldsymbol{\mathcal{C}}$ is the fourth-order, complex-valued viscoelasticity tensor field. Equation (2a) specifies a boundary condition that is homogeneous, which is assumed in this work for the sake of simplicity and without loss of generality; the case of a non-homogeneous boundary condition can be treated with minor modifications.

Here, the boundary subsets Γ_N and Γ_D are only required to not overlap (i.e., $\Gamma_N \cap \Gamma_D = \emptyset$) and do not necessarily have to form a cover of Γ (i.e., $\Gamma_N \cup \Gamma_D \subseteq \Gamma$). When they do not form a cover, equations (1a)-(3) admit a solution which is not unique, whereas a unique solution exists when $\Gamma_N \cup \Gamma_D = \Gamma$. This unusual boundary condition setting is chosen to model experimental configurations where full-field interior data (to be introduced thereafter) is available while boundary conditions are underdetermined.

Weak formulation. We denote the $L^2(\Omega)$ inner product of square-integrable second-order tensor fields \mathbf{a} and \mathbf{b} with $\langle \mathbf{a}, \mathbf{b} \rangle$:

$$\langle \mathbf{a}, \mathbf{b} \rangle := \int_{\Omega} \mathbf{a} : \bar{\mathbf{b}} \, dV = \int_{\Omega} a_{ij} \bar{b}_{ij} \, dV,$$

where the overline denotes complex conjugation and indicial notation is used (with repeated indices implying summation). The scalar product of vector or scalar fields follows the same notation, and so does the scalar product of fields defined over a surface; e.g.,

$$\langle \mathbf{a}, \mathbf{b} \rangle_\Gamma := \int_\Gamma \mathbf{a} : \bar{\mathbf{b}} \, dS.$$

The weak formulation of the balance equations (1a) and (1b) then reads

$$\langle \boldsymbol{\sigma}, \boldsymbol{\epsilon}[\mathbf{w}] \rangle - \omega^2 \langle \rho \mathbf{u}, \mathbf{w} \rangle - \langle \boldsymbol{\sigma} \cdot \mathbf{n}, \mathbf{w} \rangle_{\Gamma \setminus \Gamma_N} = \mathcal{F}(\mathbf{w}), \quad \forall \mathbf{w} \in \mathcal{W}, \quad (4)$$

with the test function space \mathcal{W} defined as $\mathcal{W} := \{\mathbf{w} : \mathbf{w} \in H^1(\Omega; \mathbb{R}^d), \mathbf{w} = 0 \text{ on } \Gamma_D\}$ and where the linear functional

$$\mathcal{F}(\mathbf{w}) = \langle \mathbf{b}, \mathbf{w} \rangle + \langle \mathbf{t}, \mathbf{w} \rangle_{\Gamma_N} \quad (5)$$

embodies the known excitations in Ω and on Γ_N . In addition, the space $\mathcal{S}(\mathbf{u})$ of dynamically admissible stresses is defined, for later reference, as

$$\mathcal{S}(\mathbf{u}) := \{\boldsymbol{\sigma} : \boldsymbol{\sigma} \in \mathcal{S}, \text{ eqn. (4) holds}\}, \quad \text{with } \mathcal{S} = L^2(\Omega; \mathbb{R}_{\text{sym}}^{3,3}). \quad (6)$$

Likewise, we define the space \mathcal{Z} of admissible viscoelasticity tensor fields as

$$\mathcal{Z} = \{\mathcal{C} \in L^\infty(\Omega; \mathcal{Q}) \mid \boldsymbol{\epsilon} : \text{Re}[\mathcal{C}(\mathbf{x})] : \boldsymbol{\epsilon} > c_0 \boldsymbol{\epsilon} : \boldsymbol{\epsilon}, \boldsymbol{\epsilon} : \text{Im}[\mathcal{C}(\mathbf{x})] : \boldsymbol{\epsilon} \geq 0 \quad \forall \mathbf{x} \in \Omega \text{ and } \boldsymbol{\epsilon} \in \mathbb{R}_{\text{sym}}^{3,3}, \boldsymbol{\epsilon} \neq 0\} \quad (7)$$

where \mathcal{Q} denotes the 21-dimensional vector space of fourth-order tensors \mathcal{C} with major and minor symmetries (i.e., $\mathcal{C}_{ijkl} = \mathcal{C}_{klij} = \mathcal{C}_{jilk}$) and c_0 is some positive constant. $\text{Re}[\cdot]$ and $\text{Im}[\cdot]$ denote the real and imaginary parts, respectively, of a complex-valued quantity. Finally, any admissible mass density field $\rho \in L^\infty(\Omega)$ must be bounded below by a positive constant.

Measurements. In addition to the fundamental equations (1a)-(3), we assume availability for the prescribed frequency ω of experimental data on steady-state displacements, namely (a) measured displacements $\tilde{\mathbf{d}}$ in $\Omega_m \subset \Omega$ (interior data) or (b) measured displacements $\tilde{\mathbf{u}}$ on $\Gamma_u \subset \Gamma$, i.e.:

$$\mathbf{u} = \tilde{\mathbf{d}} \text{ in } \Omega_m, \quad \mathbf{u} = \tilde{\mathbf{u}} \text{ on } \Gamma_u, \quad (8)$$

where Ω_m and Γ_u are not simultaneously empty (the numerical examples of Sec. 4 will emphasize the role of the interior data). Moreover, the measurement surface Γ_u is assumed to satisfy $\Gamma_D \cap \Gamma_u = \emptyset$, since obviously no displacement measurement $\tilde{\mathbf{u}}$ is needed on the constrained part of the boundary.

Remark 1. *The equality (8) between the experimental displacements $\tilde{\mathbf{d}}$ and $\tilde{\mathbf{u}}$ and their model counterparts \mathbf{u} must hold for exact measurements but will be enforced only approximately in the upcoming formulation, to account for experimental uncertainties.*

Inverse Problem. The inverse problem addressed in this work consists in reconstructing the viscoelasticity tensor field $\mathcal{C} \in \mathcal{Z}$ such that (i) the governing equations of motion (1a)-(3) are satisfied, and (ii) it is consistent with the measurement of the steady-state response of the solid for a known angular frequency ω .

3. Modified error in constitutive equation (MECE) imaging approach

3.1. MECE functional

Following the approach presented in [4, 29], the inverse problem addressed in this work is formulated as an optimization problem in which the unknown constitutive tensor \mathcal{C} is estimated by minimizing an objective function that additively combines two error terms: 1) an error in constitutive equation (ECE) functional [17] that has been adapted for viscoelastic materials and that measures the discrepancy in the constitutive equation that connects kinematically admissible strains and dynamically admissible stresses and 2) a quadratic error term that quantifies the mismatch between the predicted (or model) displacements

and the measured ones. Thus, the objective function, hereafter referred to as the viscoelasticity MECE functional, used in this work is

$$\Lambda(\mathbf{u}, \boldsymbol{\sigma}; \mathbf{C}) := U(\mathbf{u}, \boldsymbol{\sigma}; \mathbf{C}) + \frac{\kappa}{2} \left[\langle \mathbf{u} - \tilde{\mathbf{d}}, \mathbf{u} - \tilde{\mathbf{d}} \rangle_{\Omega_m} + \ell \langle \mathbf{u} - \tilde{\mathbf{u}}, \mathbf{u} - \tilde{\mathbf{u}} \rangle_{\Gamma_u} \right], \quad (9)$$

where

$$U(\mathbf{u}, \boldsymbol{\sigma}; \mathbf{C}) := \frac{1}{2} \int_{\Omega} (\boldsymbol{\sigma} - \mathbf{C} : \boldsymbol{\epsilon}[\mathbf{u}] : \mathcal{P}^{-1} : \overline{(\boldsymbol{\sigma} - \mathbf{C} : \boldsymbol{\epsilon}[\mathbf{u}])}) \, dV \quad (10)$$

is the ECE functional that has been adapted for viscoelastic materials; \mathcal{P} is a (symmetric, positive-definite, real-valued) reference fourth-order tensor used for conferring energy units to U ; $\kappa > 0$ is a weight parameter that adjusts the relative contribution of the summands to Λ in (9); and ℓ is a characteristic length (e.g. $\ell = \text{Diam}(\Omega)$) ensuring dimensional consistency. Further discussion of \mathcal{P} and κ (e.g., how to select them) is deferred to Section 3.5.

In [4, 29], where only elastic materials were considered, the choice $\mathcal{P} = \mathbf{C}$ was made in (10). Since this work is concerned with viscoelastic materials, \mathbf{C} is not in general positive-definite, so setting $\mathcal{P} = \mathbf{C}$ in (10) would fail to endow U with the following desirable properties:

$$U(\mathbf{u}, \boldsymbol{\sigma}; \mathbf{C}) \geq 0 \quad \forall \mathbf{C} \in \mathcal{Z}, \quad (11)$$

$$U(\mathbf{u}, \boldsymbol{\sigma}; \mathbf{C}) = 0 \quad \Longleftrightarrow \quad \boldsymbol{\sigma} = \mathbf{C} : \boldsymbol{\epsilon}[\mathbf{u}]. \quad (12)$$

These properties are preserved, on the other hand, by using an arbitrary symmetric, positive-definite \mathcal{P} in U . Thus, for a given triple $(\mathbf{u}, \boldsymbol{\sigma}, \mathbf{C}) \in \mathcal{W} \times \mathcal{S}(\mathbf{u}) \times \mathcal{Z}$ (see Eqs. (4,6,7) for the definition of these sets), $\Lambda(\mathbf{u}, \boldsymbol{\sigma}; \mathbf{C})$ provides a quantitative measure of the compatibility of these variables with (1) the available measurements $\tilde{\mathbf{d}}$ and $\tilde{\mathbf{u}}$ and (2) the constitutive equation. Since compatibility increases with decreasing Λ , the solution to the inverse problem of viscoelasticity imaging using an MECE approach is sought as the PDE-constrained optimization problem

$$(\mathbf{u}^*, \boldsymbol{\sigma}^*, \mathbf{C}^*) := \arg \min_{\mathbf{u} \in \mathcal{W}, \boldsymbol{\sigma} \in \mathcal{S}(\mathbf{u}), \mathbf{C} \in \mathcal{Z}} \Lambda(\mathbf{u}, \boldsymbol{\sigma}; \mathbf{C}). \quad (13)$$

A common approach for solving (13) is to use an alternating-directions strategy [11, 4, 29]. This iterative approach defines the transition from the current iterate $(\mathbf{u}, \boldsymbol{\sigma}, \mathbf{C})^n$ to the next iterate $(\mathbf{u}, \boldsymbol{\sigma}, \mathbf{C})^{n+1}$ through two successive and complementary partial minimizations of $\Lambda(\mathbf{u}, \boldsymbol{\sigma}; \mathbf{C})$. The first of these minimizations,

$$(\mathbf{u}^{n+1}, \boldsymbol{\sigma}^{n+1}) := \arg \min_{\mathbf{u} \in \mathcal{U}, \boldsymbol{\sigma} \in \mathcal{S}(\mathbf{u})} \Lambda(\mathbf{u}, \boldsymbol{\sigma}; \mathbf{C}^n), \quad (14)$$

is concerned with updating the mechanical fields \mathbf{u} and $\boldsymbol{\sigma}$ and imposes the balance of linear momentum, without the need to introduce any knowledge of external excitations or boundary conditions as a constraint, while the second minimization pertains to the update of the material parameter \mathbf{C} :

$$\mathbf{C}^{n+1} := \arg \min_{\mathbf{C} \in \mathcal{Z}} \Lambda(\mathbf{u}^{n+1}, \boldsymbol{\sigma}^{n+1}; \mathbf{C}). \quad (15)$$

The alternating-direction strategy outlined by (14) and (15) is started by choosing an initial value $\mathbf{C}^0 = \mathbf{C}_{\text{init}}$ for \mathbf{C} and performing (14) with $n = 0$.

3.2. Updating the Mechanical Fields

The partial minimization (14) is itself a PDE-constrained optimization problem. To solve it, we derive the optimality conditions using a Lagrange multiplier approach. This requires defining the Lagrangian $\mathcal{L} : \mathcal{W} \times \mathcal{W} \times \mathcal{S} \times \mathcal{Z} \rightarrow \mathbb{R}$ as

$$\mathcal{L}(\mathbf{u}, \mathbf{w}, \boldsymbol{\sigma}; \mathbf{C}) := \Lambda(\mathbf{u}, \boldsymbol{\sigma}; \mathbf{C}) + \text{Re} \left(\langle \boldsymbol{\sigma} \cdot \mathbf{n}, \mathbf{w} \rangle_{\Gamma \setminus \Gamma_N} - \langle \boldsymbol{\sigma}, \boldsymbol{\epsilon}[\mathbf{w}] \rangle + \omega^2 \langle \rho \mathbf{u}, \mathbf{w} \rangle + \mathcal{F}(\mathbf{w}) \right). \quad (16)$$

Notice the following: 1) $\mathbf{w} \in \mathcal{W}$ plays the role of the Lagrange multiplier, 2) the constraint expresses the dynamic admissibility of $\boldsymbol{\sigma}$ inherent to the definition (6) of $\mathcal{S}(\mathbf{u})$, and 3) the term $\langle \boldsymbol{\sigma} \cdot \mathbf{n}, \mathbf{w} \rangle_{\Gamma \setminus \Gamma_N}$ in (16) is crucial for the case in which $\Gamma_N \cup \Gamma_D \neq \Gamma$ (i.e., boundary conditions are not prescribed over the entire boundary).

In order to derive the optimality conditions, the derivatives of \mathcal{L} with respect to \mathbf{u} , \mathbf{w} , and $\boldsymbol{\sigma}$ need to be computed. This is done by means of the directional (Gâteaux) derivative. The Gâteaux derivative $F'_g(\delta g)$ of a functional F with respect to g in the direction δg is defined as

$$F'_g(\delta g) := \left. \frac{d}{d\epsilon} F(g + \epsilon \delta g) \right|_{\epsilon=0}.$$

With this definition, the derivative of \mathcal{L} with respect to $\boldsymbol{\sigma}$ in the direction $\delta \boldsymbol{\sigma} \in \mathcal{S}$ is

$$\begin{aligned} \mathcal{L}'_{\boldsymbol{\sigma}}(\delta \boldsymbol{\sigma}) &= \text{Re} \left(\langle \delta \boldsymbol{\sigma}, \mathcal{P}^{-1} : \boldsymbol{\sigma} \rangle - \langle \delta \boldsymbol{\sigma}, \mathcal{P}^{-1} : \mathcal{C} : \boldsymbol{\epsilon}[\mathbf{u}] \rangle - \langle \delta \boldsymbol{\sigma}, \boldsymbol{\epsilon}[\mathbf{w}] \rangle + \langle \delta \boldsymbol{\sigma} \cdot \mathbf{n}, \mathbf{w} \rangle_{\Gamma \setminus \Gamma_N} \right) \\ &= \text{Re} \left(\langle \delta \boldsymbol{\sigma}, \mathcal{P}^{-1} : (\boldsymbol{\sigma} - \mathcal{C} : \boldsymbol{\epsilon}[\mathbf{u}]) - \boldsymbol{\epsilon}[\mathbf{w}] \rangle + \langle \delta \boldsymbol{\sigma} \cdot \mathbf{n}, \mathbf{w} \rangle_{\Gamma \setminus \Gamma_N} \right). \end{aligned} \quad (17)$$

Enforcing the stationarity condition $\mathcal{L}'_{\boldsymbol{\sigma}}(\delta \boldsymbol{\sigma}) = 0 \ \forall \delta \boldsymbol{\sigma} \in \mathcal{S}$, we obtain from (17)

$$\mathbf{w} = \mathbf{0} \quad \text{on } \Gamma \setminus \Gamma_N, \quad (18a)$$

$$\boldsymbol{\sigma} = \mathcal{C} : \boldsymbol{\epsilon}[\mathbf{u}] + \mathcal{P} : \boldsymbol{\epsilon}[\mathbf{w}] \quad \text{in } \Omega. \quad (18b)$$

Equation (18a) implies that $\mathbf{w} \in \mathcal{W}_0 \subseteq \mathcal{W}$, with the function space \mathcal{W}_0 defined as

$$\mathcal{W}_0 := \{ \mathbf{w} : \mathbf{w} \in \mathcal{W}, \mathbf{w} = \mathbf{0} \text{ on } \Gamma \setminus \Gamma_N \}. \quad (19)$$

Note that $\mathcal{W}_0 \subset \mathcal{W}$ (with strict inclusion) whenever the boundary data is insufficient (i.e. $\Gamma_N \cup \Gamma_D \neq \Gamma$), while $\mathcal{W}_0 = \mathcal{W}$ when $\Gamma_N \cup \Gamma_D = \Gamma$ (sufficient boundary data). Then, proceeding in a similar manner, the derivative of \mathcal{L} with respect to \mathbf{u} in the direction $\delta \mathbf{u} \in \mathcal{W}$ is

$$\begin{aligned} \mathcal{L}'_{\mathbf{u}}(\delta \mathbf{u}) &= \text{Re} \left(\langle (\mathcal{C} : \boldsymbol{\epsilon}[\mathbf{u}] - \boldsymbol{\sigma}) : \mathcal{P}^{-1} : \bar{\mathcal{C}}, \boldsymbol{\epsilon}[\delta \mathbf{u}] \rangle \right. \\ &\quad \left. + \kappa \left(\langle \mathbf{u} - \tilde{\mathbf{d}}, \delta \mathbf{u} \rangle_{\Omega_m} + \ell \langle \mathbf{u} - \tilde{\mathbf{u}}, \delta \mathbf{u} \rangle_{\Gamma_u} \right) + \omega^2 \langle \rho \delta \mathbf{u}, \mathbf{w} \rangle \right). \end{aligned} \quad (20)$$

After substituting (18b) into (20), the stationarity condition $\mathcal{L}'_{\mathbf{u}}(\delta \mathbf{u}) = 0 \ \forall \delta \mathbf{u} \in \mathcal{W}$ takes the form

$$\langle \bar{\mathcal{C}} : \boldsymbol{\epsilon}[\mathbf{w}], \boldsymbol{\epsilon}[\delta \mathbf{u}] \rangle - \omega^2 \langle \rho \mathbf{w}, \delta \mathbf{u} \rangle = \kappa \left(\langle \mathbf{u} - \tilde{\mathbf{d}}, \delta \mathbf{u} \rangle_{\Omega_m} + \ell \langle \mathbf{u} - \tilde{\mathbf{u}}, \delta \mathbf{u} \rangle_{\Gamma_u} \right) \quad \forall \delta \mathbf{u} \in \mathcal{W}. \quad (21)$$

Following the same steps for the remaining stationarity condition (which is the constraint in (16)) yields, using (18b) and noting that $\langle \boldsymbol{\sigma} \cdot \mathbf{n}, \delta \mathbf{w} \rangle_{\Gamma \setminus \Gamma_N}$ vanishes because $\delta \mathbf{w} \in \mathcal{W}_0$:

$$\langle \mathcal{C} : \boldsymbol{\epsilon}[\mathbf{u}] + \mathcal{P} : \boldsymbol{\epsilon}[\mathbf{w}], \boldsymbol{\epsilon}[\delta \mathbf{w}] \rangle - \omega^2 \langle \rho \mathbf{u}, \delta \mathbf{w} \rangle = \mathcal{F}(\delta \mathbf{w}) \quad \forall \delta \mathbf{w} \in \mathcal{W}_0. \quad (22)$$

For a given $\mathcal{C}^n \in \mathcal{Z}$ at the n^{th} iteration of the alternating directions scheme, the mechanical field update thus corresponds to finding $(\mathbf{u}, \mathbf{w})^{n+1} \in \mathcal{W} \times \mathcal{W}_0$ solving problem $\mathcal{P}(\mathbf{u}^{n+1}, \mathbf{w}^{n+1}; \mathcal{C}^n)$, where problem $\mathcal{P}(\mathbf{u}, \mathbf{w}; \mathcal{C})$ is defined by the coupled weak formulation

$$\begin{aligned} \langle \bar{\mathcal{C}} : \boldsymbol{\epsilon}[\mathbf{w}], \boldsymbol{\epsilon}[\delta \mathbf{u}] \rangle - \omega^2 \langle \rho \mathbf{w}, \delta \mathbf{u} \rangle - \kappa \mathcal{A}(\mathbf{u}, \delta \mathbf{u}) &= -\kappa \mathcal{A}_m(\delta \mathbf{u}) \quad \forall \delta \mathbf{u} \in \mathcal{W}, \\ \langle \mathcal{P} : \boldsymbol{\epsilon}[\mathbf{w}], \boldsymbol{\epsilon}[\delta \mathbf{w}] \rangle + \langle \mathcal{C} : \boldsymbol{\epsilon}[\mathbf{u}], \boldsymbol{\epsilon}[\delta \mathbf{w}] \rangle - \omega^2 \langle \rho \mathbf{u}, \delta \mathbf{w} \rangle &= \mathcal{F}(\delta \mathbf{w}) \quad \forall \delta \mathbf{w} \in \mathcal{W}_0, \end{aligned} \quad (23)$$

with

$$\mathcal{A}(\mathbf{u}, \delta \mathbf{u}) := \langle \mathbf{u}, \delta \mathbf{u} \rangle_{\Omega_m} + \ell \langle \mathbf{u}, \delta \mathbf{u} \rangle_{\Gamma_u}, \quad \mathcal{A}_m(\delta \mathbf{u}) := \langle \tilde{\mathbf{d}}, \delta \mathbf{u} \rangle_{\Omega_m} + \ell \langle \tilde{\mathbf{u}}, \delta \mathbf{u} \rangle_{\Gamma_u}.$$

After solving (23) for $(\mathbf{u}, \mathbf{w}) = (\mathbf{u}^{n+1}, \mathbf{w}^{n+1})$, the stress $\boldsymbol{\sigma}^{n+1}$ can be computed using (18b) with $\mathcal{C} = \mathcal{C}^n$.

3.3. Updating the Material Properties

The next step in the alternating directions scheme is to solve the inequality-constrained optimization subproblem (15), referred to as the material update step. Given the nature of the admissibility constraints imposed on the viscoelasticity tensor fields, see (7), the material update $\mathcal{C}^{n+1} \in \mathcal{Z}$ is here computed by means of the following two substeps:

1. *Proposal substep*: A proposed material update $\tilde{\mathcal{C}}^{n+1}$ is computed by enforcing the first-order necessary optimality condition $\mathcal{L}'_{\mathcal{C}}(\delta \mathcal{C}) = 0 \ \forall \delta \mathcal{C} \in \mathcal{Z}$.
2. *Correction substep*: If $\tilde{\mathcal{C}}^{n+1}$ is admissible, then $\mathcal{C}^{n+1} := \tilde{\mathcal{C}}^{n+1}$. Otherwise, a correction procedure (explained shortly thereafter) determines an admissible update \mathcal{C}^{n+1} that approximates $\tilde{\mathcal{C}}^{n+1}$.

Proposal substep. Enforcing the condition $\mathcal{L}'_{\mathcal{C}}(\delta\mathcal{C}) = 0 \ \forall \delta\mathcal{C} \in \mathcal{Z}$, $\tilde{\mathcal{C}}^{n+1}$ solves

$$\forall \delta\mathcal{C} \in \mathcal{Z}, \left\langle \left(\tilde{\mathcal{C}}^{n+1} : \epsilon[\mathbf{u}^{n+1}] - \boldsymbol{\sigma}^{n+1} \right) : \mathcal{P}^{-1}, \epsilon[\bar{\mathbf{u}}^{n+1}] : \delta\mathcal{C} \right\rangle = 0. \quad (24)$$

We will focus on isotropic materials for the rest of this article as they lead to simple updating formulae in the MECE context as shown next. Thus, \mathcal{C} has the form

$$\mathcal{C} = \left(B - \frac{2}{3}G \right) (\mathbf{I} \otimes \mathbf{I}) + 2G\mathcal{I} \quad (25)$$

with B and G denoting (spatially-dependent) bulk and shear complex moduli, respectively. \mathbf{I} and \mathcal{I} are the second- and fourth-order identity tensors, respectively. The tensor \mathcal{P} is then also assumed to be isotropic and to have the same major and minor symmetries as \mathcal{C} . Hence, \mathcal{P} can be represented as

$$\mathcal{P} = \left(B_p - \frac{2}{3}G_p \right) (\mathbf{I} \otimes \mathbf{I}) + 2G_p\mathcal{I}, \quad (26)$$

where G_p and B_p are real, positive constants whose selection is discussed in Section 3.5.

The formulae for the proposed update are obtained by first decoupling the stress and strain tensors into deviatoric and volumetric components; i.e.,

$$\boldsymbol{\sigma} = \boldsymbol{\sigma}_{\text{dev}} + q\mathbf{I}, \quad \epsilon[\mathbf{u}] = \epsilon_{\text{dev}}[\mathbf{u}] + \frac{1}{3}e_u\mathbf{I},$$

where $\boldsymbol{\sigma}_{\text{dev}}$ and ϵ_{dev} are the deviatoric stress and strain tensors, respectively, $q = \frac{1}{3}\text{tr}(\boldsymbol{\sigma})$ is the mean stress, and $e_u = \text{tr}(\epsilon[\mathbf{u}])$ is the volumetric strain. Then, combining (24), (25), and (26) and considering variations $\delta\mathcal{C}$ having the form (25) yields

$$\left\langle \frac{1}{2G_p} \left(2\tilde{G}^{n+1}\epsilon_{\text{dev}}[\mathbf{u}^{n+1}] - \boldsymbol{\sigma}_{\text{dev}}^{n+1} \right) : \epsilon_{\text{dev}}[\bar{\mathbf{u}}^{n+1}], \delta G \right\rangle + \left\langle \frac{e_u^{n+1}}{B_p} \left(\tilde{B}^{n+1}e_u^{n+1} - q^{n+1} \right), \delta B \right\rangle = 0 \quad \forall \delta G, \delta B, \quad (27)$$

This implies the following pointwise update proposal formulae for the bulk and shear moduli:

$$\tilde{B}^{n+1} = \frac{q^{n+1}}{e_u^{n+1}} = \frac{\text{tr}(\boldsymbol{\sigma}^{n+1})}{3\text{tr}(\epsilon[\mathbf{u}^{n+1}])}, \quad \tilde{G}^{n+1} = \frac{\boldsymbol{\sigma}_{\text{dev}}^{n+1} : \epsilon_{\text{dev}}[\bar{\mathbf{u}}^{n+1}]}{2\epsilon_{\text{dev}}[\mathbf{u}^{n+1}] : \epsilon_{\text{dev}}[\bar{\mathbf{u}}^{n+1}]}. \quad (28)$$

The formulae (28) can be easily extended to the case where B and G are assumed to be constant over some region $D \subseteq \Omega$. In this case, the numerators and denominators in (28) carry implicit integrations over D ; i.e.,

$$\tilde{B}^{n+1} = \frac{\langle \boldsymbol{\sigma}^{n+1}, \mathbf{I} \rangle_D}{3 \langle \epsilon[\mathbf{u}^{n+1}], \mathbf{I} \rangle_D}, \quad \tilde{G}^{n+1} = \frac{\langle \boldsymbol{\sigma}_{\text{dev}}^{n+1}, \epsilon_{\text{dev}}[\bar{\mathbf{u}}^{n+1}] \rangle_D}{2 \langle \epsilon_{\text{dev}}[\mathbf{u}^{n+1}], \epsilon_{\text{dev}}[\bar{\mathbf{u}}^{n+1}] \rangle_D}. \quad (29)$$

Correction substep. The proposed material updates (28) may not satisfy the inequality constraints imposed by \mathcal{Z} [8]. Thus, the actual updates B^{n+1} and G^{n+1} are in this work defined from the proposals $\tilde{B}^{n+1}, \tilde{G}^{n+1}$ by means of the correction rule

$$h(X^{n+1}) := \begin{cases} h(\tilde{X}^{n+1}) & : h(X_{\text{low}}) \leq h(\tilde{X}^{n+1}) \leq h(X_{\text{up}}) \\ h(\theta X^n + (1-\theta)X_{\text{low}}) & : h(\tilde{X}^{n+1}) < h(X_{\text{low}}) \\ h(\theta X^n + (1-\theta)X_{\text{up}}) & : h(\tilde{X}^{n+1}) > h(X_{\text{up}}) \end{cases}, \quad (30)$$

where X stands for either B or G , the function $h(\cdot)$ is to be substituted with either $\text{Re}(\cdot)$ or $\text{Im}(\cdot)$, and $\theta \in [0, 1]$ is a user-defined weight ($\theta = 0.5$ for the examples shown in Section 4). The complex numbers B_{low} and B_{up} (respectively, G_{low} and G_{up}) are prescribed a priori and serve as lower and upper bounds for B (respectively, G): whenever the real (imaginary) part of the proposed update falls outside of the allowable interval, it is replaced with a weighted average of the real (imaginary) part of the previous estimate and the bound being violated. The material update rule (30) may be made equivalent to the gradient projection method by replacing the correction substep with a subspace minimization (see [19, p. 488] for details), a variation not used here.

Remark 2. *The treatment of anisotropic materials may require approaches different from the simple updating formulae shown herein depending on the level of material symmetry considered (See Reference [6] for instance). On the other hand, gradient-based algorithms could be used in general in MECE without any limitation regarding material symmetries. This direction is currently being investigated by the authors.*

3.4. Discretization

The finite element method was used in this work to approximate the solution of the governing variational problems. Using standard Voigt notation, the trial and test functions and their derivatives are expressed as

$$\begin{aligned} \mathbf{u}^h &= [N] \{u\}, & \delta \mathbf{u}^h &= [N] \{\delta u\}, & \boldsymbol{\epsilon}[\mathbf{u}^h] &= [B] \{u\}, \\ \mathbf{w}^h &= [N] \{w\}, & \delta \mathbf{w}^h &= [N] \{\delta w\}, & \boldsymbol{\epsilon}[\mathbf{w}^h] &= [B] \{w\}, \end{aligned}$$

where $[N]$ and $[B]$ represent matrices of finite element shape functions and their derivatives with respect to spatial coordinates, respectively. Moreover, the viscoelasticity field \mathcal{C} is discretized using piecewise constant basis functions (i.e., \mathcal{C} is assumed to be constant in each element).

After substituting the above approximations into (23) and applying the standard finite element method, the discrete coupled system of equations is obtained as

$$\begin{bmatrix} [T] & [K] - \omega^2 [M] \\ ([K] - \omega^2 [M])^H & -\kappa [D] \end{bmatrix} \begin{Bmatrix} \{w\} \\ \{u\} \end{Bmatrix} = \begin{Bmatrix} \{F\} \\ -\kappa \{R\} \end{Bmatrix}, \quad (31)$$

where the superscript notation used to denote an iteration within the alternating directions scheme has been dropped for the sake of clarity. The matrices and vectors in the block system (31) are defined as follows:

$$[K] := \sum_{\text{elements}} \int_{\Omega^e} [B]^T [C] [B] \, dV \quad (32a)$$

$$[T] := \sum_{\text{elements}} \int_{\Omega^e} [B]^T [P] [B] \, dV \quad (32b)$$

$$[M] := \sum_{\text{elements}} \int_{\Omega^e} \rho [N]^T [N] \, dV \quad (32c)$$

$$[D] := \sum_{\text{elements}} \int_{\Omega_m^e} [N]^T [N] \, dV + \sum_{\text{elements}} \int_{\Gamma_u^e} [N]^T [N] \, dS \quad (32d)$$

$$\{F\} := \sum_{\text{elements}} \int_{\Gamma_N^e} [N]^T \mathbf{t} \, dS + \sum_{\text{elements}} \int_{\Omega^e} [N]^T \mathbf{b} \, dV \quad (32e)$$

$$\{R\} := \sum_{\text{elements}} \int_{\Omega_m^e} [N]^T \tilde{\mathbf{d}} \, dV + \sum_{\text{elements}} \int_{\Gamma_u^e} [N]^T \tilde{\mathbf{u}} \, dS. \quad (32f)$$

$[C]$ and $[P]$ denote the appropriate matrix representations of the fourth-order tensors \mathcal{C} and \mathcal{P} , respectively. Moreover, the coefficient matrix in (31) is Hermitian. The measured displacements $\tilde{\mathbf{d}}$ and $\tilde{\mathbf{u}}$ in (32f) are assumed to be continuous over (i.e. available at all nodes in) their respective measurement regions. However, cases where the measurement data is sparse can be easily taken into consideration. In this case, measurement locations can be made to coincide with finite element nodes, and $[D]$ in (31) is replaced by a diagonal Boolean matrix $[Q]$ with nonzero entries only for those global degrees of freedom (DOFs) that are measured; moreover, $\{R\}$ becomes a vector whose entries are the measured displacements at the different DOFs. For this work, the system (31) was solved using the parallel, sparse direct linear solver PARDISO [26, 27].

We now explore the unique solvability of the block system (31). Let $[A] := [K] - \omega^2 [M]$ and assume that $\Gamma_N \neq \Gamma$ (i.e., not all of the boundary Γ has a natural boundary condition such as (1b)). The latter condition makes $[T]$ positive definite and, hence, invertible. Let $\{u\}$ and $\{w\}$ be elements of the kernel of the coefficient matrix in (31), i.e. such that

$$\begin{aligned} [T]\{w\} + [A]\{u\} &= \{0\} \\ [A]^H \{w\} - \kappa [D]\{u\} &= \{0\}. \end{aligned}$$

Combining the above equations and using the invertibility of $[T]$ so as to eliminate $\{w\}$, $\{u\}$ is found to verify

$$([A]^H [T]^{-1} [A] + \kappa [D]) \{u\} = \{0\}.$$

Since $[A]^H [T]^{-1} [A]$ and $[D]$ are both symmetric and semi-definite positive, this implies that $\{u\}$ must satisfy both $[A]^H [T]^{-1} [A] \{u\} = \{0\}$ and $[D] \{u\} = \{0\}$. Consequently, the kernel of the block matrix in (31) is trivial (i.e., $\{u\} = \{w\} = \{0\}$) only if

$$\text{Ker}([A]^H [T]^{-1} [A]) \cap \text{Ker}([D]) = \{0\}, \quad (33)$$

where $\text{Ker}(\cdot)$ denotes the kernel of a matrix. Since $[T]$ is positive definite, condition (33) reduces to $\text{Ker}([A]) \cap \text{Ker}([D]) = \{0\}$. This analysis does not hold in the case where $\Gamma_N = \Gamma$, which is deemed here of little relevance for interior data problems.

Remark 3. Importantly, the inclusion $\mathcal{W}_0 \subset \mathcal{W}$ implies that $[A]$ is rectangular, with more columns than rows, unless sufficient boundary conditions are present. In that case, $\text{Ker}([A])$ is nontrivial, and condition (33) imposes constraints on experiments in order to ensure invertibility of the coupled system (31). Those constraints may be understood as requiring the amount of internal measurements to at least compensate the missing boundary data. They are for example largely satisfied in the examples of Section 4, where boundary conditions are absent over the entire boundary but a measured displacement field is assumed to be available either over the whole domain or in a significant portion of it (full-field data). For instance, in the former case, the observation matrix $[D]$ is positive definite (i.e. $\text{Ker}([D]) = \{0\}$), which ensures invertibility of (31) as per (33).

Remark 4. The fact that the discrete stationarity system (31) is found to be uniquely solvable subject only to the relatively mild condition (33) is important, as it makes the proposed MECE-based identification method applicable to many boundary condition and measurement setups.

3.5. The scaling tensor \mathcal{P} and the penalty term κ

Choosing \mathcal{P} . We chose to define \mathcal{P} in terms of the initial viscoelasticity tensor $\mathcal{C}_{\text{init}}$ by $\mathcal{P} = \beta_R \text{Re}[\mathcal{C}_{\text{init}}] + \beta_I \text{Im}[\mathcal{C}_{\text{init}}]$, with positive weights β_R, β_I . This choice satisfies the properties required of \mathcal{P} , namely that it be a real-valued, symmetric, positive definite fourth-order tensor (see Sec. 3.1) independent on the unknown \mathcal{C} . Letting $[K_{\text{init};R}]$ and $[K_{\text{init};I}]$ denote the real and imaginary parts of the initial stiffness matrix, defined by (32a) with $[C]$ replaced by $[C_{\text{init}}]$, the matrix $[T]$ defined in (32b) is then given by $[T] = \beta_R [K_{\text{init};R}] + \beta_I [K_{\text{init};I}]$ (up to differences related to the fact that $[K_{\text{init}}]$ and $[T]$ incorporate kinematic constraints associated to spaces \mathcal{W} and \mathcal{W}_0 , respectively). We explored different values for the weights β_R and β_I through numerical experiments and found the algorithm to be robust in this respect. The arbitrary choice $\beta_R = \beta_I = 1$ was used for all results reported thereafter.

Choosing κ . The parameter κ in (9) weights the relative importance between minimizing the ECE term and matching the experimental data and thus affects the quality of the reconstruction of \mathcal{C} . As it affects the smoothness of \mathcal{C} , it acts in this sense as a regularizer, its exact role being (as discussed in [29]) reciprocal to that of a conventional Tikhonov regularization parameter.

As a first step, the following form for κ , originally proposed in [4], is used as

$$\kappa := \alpha A, \quad A := \frac{\langle \epsilon[\mathbf{u}_{\text{init}}], \mathcal{P} : \epsilon[\mathbf{u}_{\text{init}}] \rangle}{\langle \tilde{\mathbf{d}}, \tilde{\mathbf{d}} \rangle_{\Omega_m} + \ell \langle \tilde{\mathbf{u}}, \tilde{\mathbf{u}} \rangle_{\Gamma_u}}, \quad (34)$$

where the weight parameter $\alpha > 0$ is dimensionless and \mathbf{u}_{init} solves equations (1a)-(3) with $\mathcal{C} = \mathcal{C}_{\text{init}}$. If $\Gamma \setminus (\Gamma_D \cup \Gamma_N) \neq \emptyset$, it is necessary to prescribe arbitrarily chosen boundary conditions in order to define \mathbf{u}_{init} uniquely. This does not affect the generality of the method, as \mathbf{u}_{init} is used only as a means to scale κ . Notice that (34) makes the components of Λ in (9) dimensionally consistent, each having units of energy.

The next step is to devise a strategy for the selection of α . Appropriately choosing α is critical because high values of α will result in low values of the displacement-misfit functionals in (9), which is undesirable in the case of noisy data. Conversely, too-low values of α will result in high values of the displacement-misfit functionals, entailing potential loss of important information contained in the measurements and the over-smoothing of the solution to the inverse problem.

The selection of α in this work is based on Morozov’s discrepancy principle [9, 16], a well-established approach which assumes the level of noise δ in the measurement data to be known *a priori*. This principle dictates that the parameter α be chosen to be the smallest positive number such that the final discrepancy between the computed and measured system response is within the noise level. That is, we select the minimum α possible subject to the condition

$$\left| \frac{\langle \mathbf{u}_\alpha - \tilde{\mathbf{d}}, \mathbf{u}_\alpha - \tilde{\mathbf{d}} \rangle_{\Omega_m} + \ell \langle \mathbf{u}_\alpha - \tilde{\mathbf{u}}, \mathbf{u}_\alpha - \tilde{\mathbf{u}} \rangle_{\Gamma_u} - \delta^2}{\langle \tilde{\mathbf{d}}, \tilde{\mathbf{d}} \rangle_{\Omega_m} + \ell \langle \tilde{\mathbf{u}}, \tilde{\mathbf{u}} \rangle_{\Gamma_u}} \right| \leq \epsilon_m \delta^2, \quad (35)$$

where \mathbf{u}_α denotes the displacement field obtained as a solution to the optimality system (13) with $\kappa = \alpha A$ and ϵ_m is a specified relative tolerance. A simple bisection method was implemented to find α on the basis of (35). This requires solving at each bisection step the optimization problem (13) (here, by means of the proposed alternating directions scheme). A tolerance $\epsilon_m = O(10^{-2})$ was found to be adequate for the examples of Section 4. Lower error tolerances did not yield any noticeable differences in the solution.

4. Numerical Experiments

This section is devoted to a series of numerical experiments, inspired by the field of biomedical imaging, that are intended to showcase the capabilities of the methodology of Section 3. They consist in imaging a viscoelastic inclusion (with unknown location, geometry, and characteristics) embedded in a viscoelastic background medium (all materials being assumed to be isotropic) by reconstructing the complex bulk and shear moduli fields B and G , treated as completely unknown. In particular, the examples demonstrate that adequate reconstructions are achieved in situations where information on the boundary conditions is absent. In Example 1, a two-dimensional problem is considered where B and G are estimated using noisy interior displacement data with boundary conditions either known or unknown. Example 2 uses the same setup as Example 1, but the reconstruction of B and G is done in a window of the problem domain. In Example 3, B and G are imaged in a three-dimensional domain using a full displacement field. In all examples, frequencies were chosen so as to maintain low wavenumbers in the domain. This choice was made without loss of generality and in the interest of avoiding excessively fine meshes.

Synthetic measurements were generated for all examples by (i) performing a finite element simulation with the target material parameters, using a dedicated data simulation mesh; (ii) interpolating the resulting displacement field onto a (different) reconstruction mesh; and (iii) corrupting that interpolated field with random noise. For the simulated displacement \hat{u}_i at a node i , the corresponding noisy measurement \tilde{u}_i is given as

$$\tilde{u}_i = \hat{u}_i(1 + \delta r_i), \quad (36)$$

where r_i is a normal random variable with zero mean and unit variance and the parameter δ is a prescribed relative noise level. In our examples, we use $\delta = 0.01$ and 0.05 . The reconstruction mesh in step (ii) is introduced in order to avoid committing the “inverse crime” in evaluating an inversion methodology; it is regular (so it carries no information about the inclusion geometry) and coarser than the data simulation mesh.

For all examples, $(B_{\text{init}}, G_{\text{init}})$ will denote (homogeneous) initial guesses, and (B^*, G^*) will represent the complex moduli fields yielded by the MEQR-based reconstruction. (B_0, G_0) , (B_1, G_1) will indicate target values for the background and inclusion materials, respectively, and $(B^{\text{ref}}, G^{\text{ref}})$ will denote the corresponding target moduli fields. Moreover, all materials used in the examples have a homogeneous mass density $\rho = 1,000 \text{ kg/m}^3$. All discretized moduli fields are defined with reference to the reconstruction mesh, with G^{ref} and B^{ref} initially defined on the data simulation mesh and then projected to the reconstruction mesh. The relative L^p errors on moduli reconstructions will be evaluated (with $p = 1$ or 2 , and using the reconstruction mesh) for each example; they are defined by

$$e_p[X] := \left[\frac{\int_{\Omega} |X^* - X^{\text{ref}}|^p \, dV}{\int_{\Omega} |X^{\text{ref}}|^p \, dV} \right]^{1/p}, \quad (p = 1, 2; \ X = B, G). \quad (37)$$

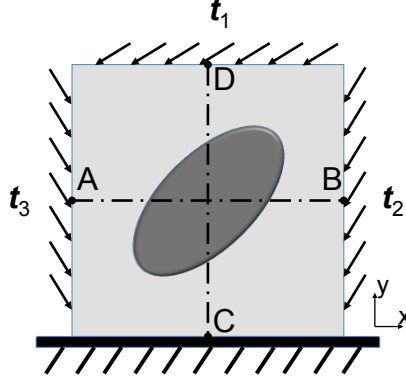


Figure 1: Diagram of the problem domain in Examples 1 and 2

For this work, the alternating directions scheme was stopped and deemed to have converged when the relative change in the functional (9) between two successive iterations dropped below 0.1% for Examples 1 and 2 and 1% for Example 3. A higher tolerance was selected for Example 3 to avoid excessively long computation times. As pointed out in [29], this criterion was confirmed to be adequate for the examples presented herein as it was verified (from extensive numerical testing) that the relative change in the mechanical fields and moduli was negligible for these levels of change in the functional.

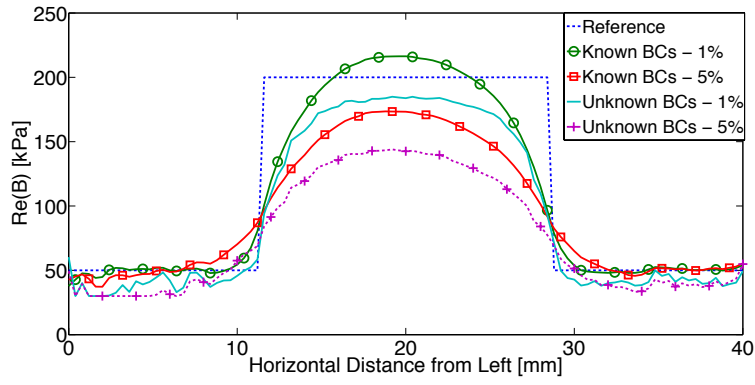
4.1. Example 1: 2D reconstruction with 2D data

This example demonstrates the ability of the proposed methodology to image the shear and bulk moduli fields of viscoelastic materials from noisy two-dimensional displacement data, under plane strain conditions. Two scenarios were considered. Scenario 1 assumes complete knowledge of the boundary conditions (i.e., $\Gamma_D \cup \Gamma_N = \Gamma$), whereas Scenario 2 assumes no knowledge of the boundary conditions (i.e., $\Gamma_D = \Gamma_N = \emptyset$). The domain for this example (Fig. 1) consists of a square background with an elliptical inclusion. Each side of the square is 4 cm, and the ellipse has a major radius, respectively minor radius, of $8\sqrt{2}$ mm, respectively $5\sqrt{2}$ mm. Moreover, the major radius of the ellipse has an orientation of 45° with respect to the x -axis.

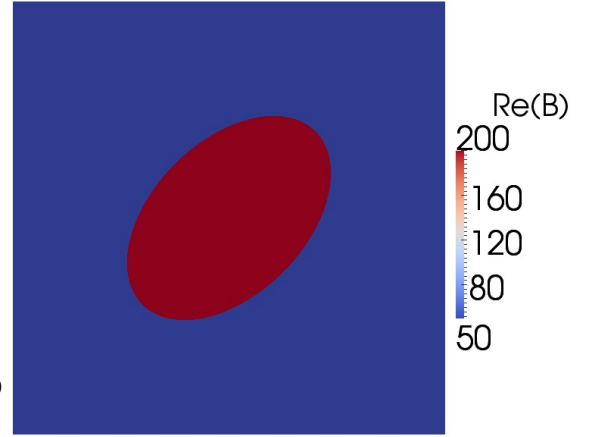
The frequency used in this example was 100 Hz. The target viscoelastic moduli for the background were set to $B_0 = 50$ kPa and $G_0 = 5 + 2.5i$ kPa (with $i = \sqrt{-1}$), with the inclusion target properties taken as $B_1 = 4B_0$ and $G_1 = 4G_0$. The bulk modulus was thus assumed to be purely elastic. There are many applications in which the bulk modulus is taken as purely elastic (see for instance [12, 14]). The boundary conditions used to generate the measurement data, sketched in Figure 1, were such that the bottom side was fixed while traction loads given by $\mathbf{t}_1 = [0 \ -5]$ kPa, $\mathbf{t}_2 = [-5 \ 5]$ kPa, and $\mathbf{t}_3 = [5 \ -5]$ kPa (see Fig. 1) were applied to all other sides. The data simulation mesh involved about 22,000 linear quadrilateral (Q4) elements, while the reconstruction mesh used 15,600 Q4 elements. Moreover, the noise levels used in (36) were $\delta = 0.01$ and 0.05 .

The alternating directions algorithm was started by setting $(B_{\text{init}}, G_{\text{init}}) = (B_0, G_0)$. Figure 2 shows $\text{Re}(B^*)$, the real part of the reconstructed bulk modulus. The background modulus is seen to be correctly preserved in all four cases. Moreover, the inclusion shape was also accurately recovered. The accuracy of the reconstruction B^* in the inclusion, however, varies according to the data noise and whether boundary conditions are known or unknown: unsurprisingly, the reconstruction with $\delta = 0.01$ is more accurate than that with $\delta = 0.05$, while the lack of boundary condition data also moderately degrades accuracy. Indeed, all images in Figure 2 correctly reveal the stiffer inclusion.

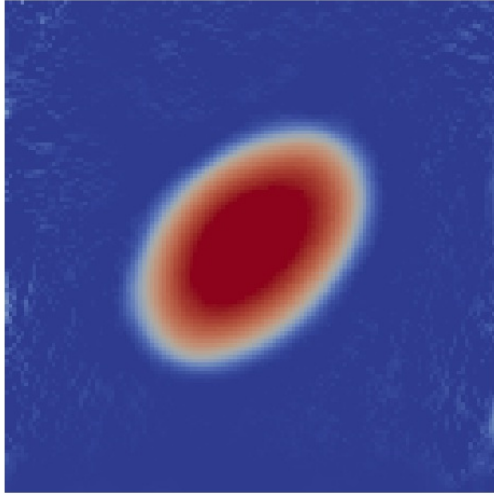
The imaging results $\text{Re}(G^*)$ and $\text{Im}(G^*)$ are shown in Figures 3 and 4, respectively. Trends similar to the results for $\text{Re}(B^*)$ can again be observed. The reconstruction of $\text{Im}(G)$ appears to be less accurate than that of the other quantities. This can be explained by the sensitivity of $\text{Im}(G^*)$ on the measured data, since different reconstructions (not reported herein) were obtained using data generated with different loading conditions.



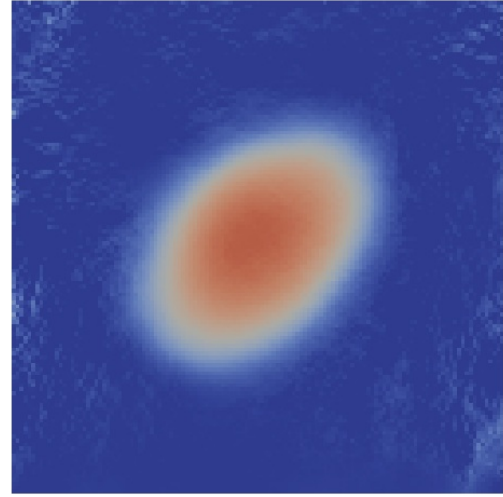
(a) Line plot along AB (see Fig. 1)



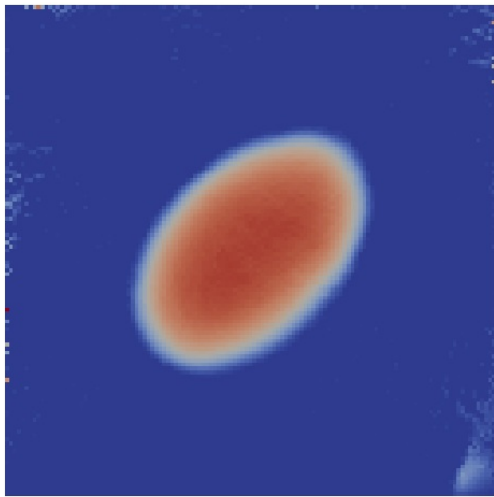
(b) Reference B^{ref}



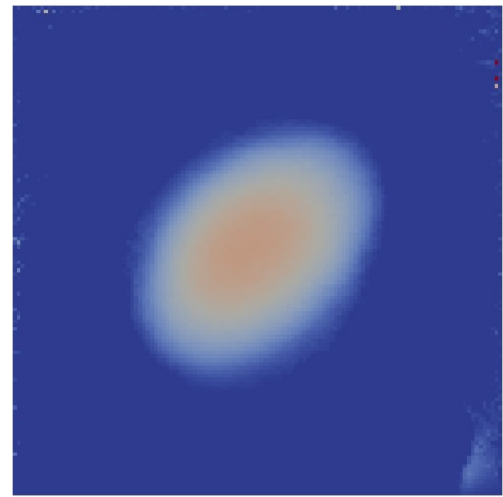
(c) $\text{Re}(B^*)$: known BCs, $\delta = 0.01$



(d) $\text{Re}(B^*)$: known BCs, $\delta = 0.05$

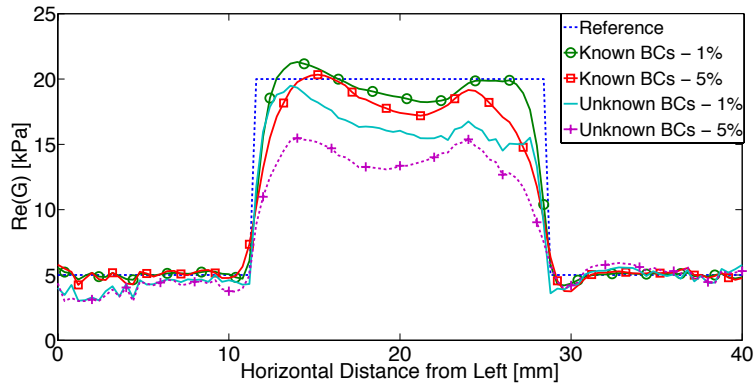


(e) $\text{Re}(B^*)$: unknown BCs, $\delta = 0.01$

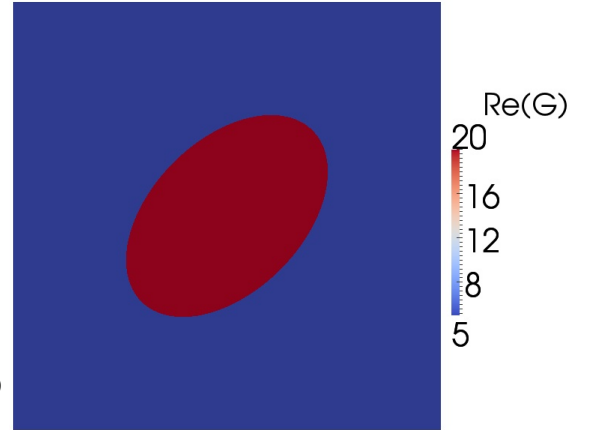


(f) $\text{Re}(B^*)$: unknown BCs, $\delta = 0.05$

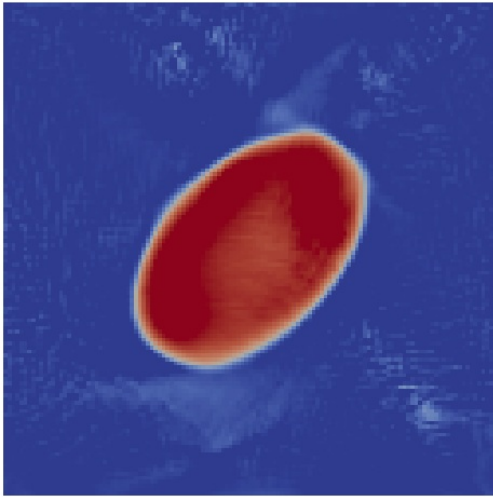
Figure 2: Example 1, reconstruction of $\text{Re}(B)$. Units: kPa, mm



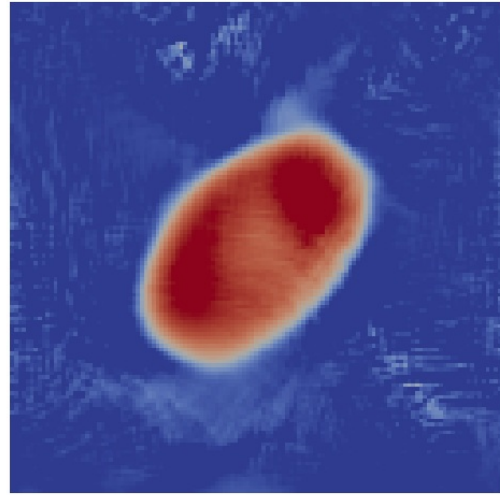
(a) Line plot along AB (see Fig. 1)



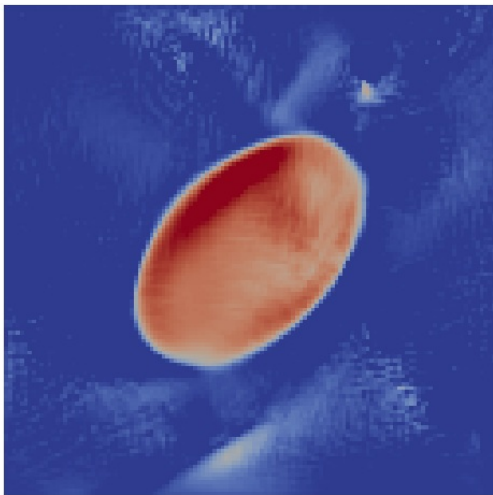
(b) Reference $\text{Re}(G^{\text{ref}})$



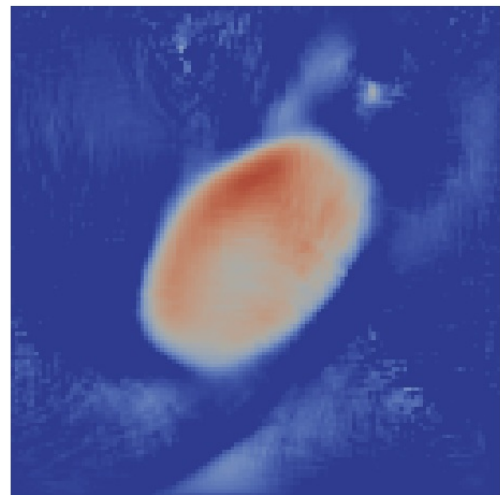
(c) $\text{Re}(G^*)$: known BCs, $\delta = 0.01$



(d) $\text{Re}(G^*)$: known BCs, $\delta = 0.05$

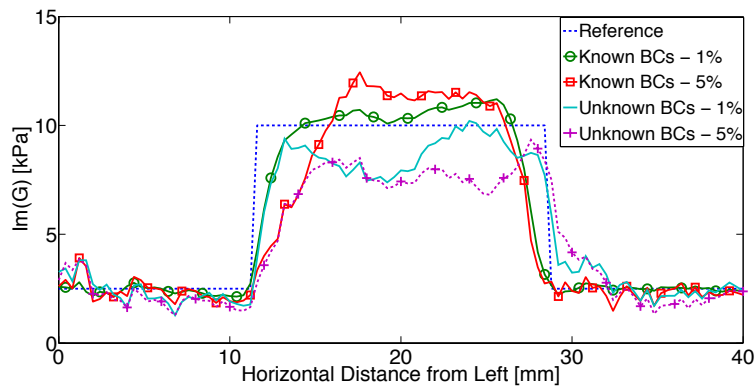


(e) $\text{Re}(G^*)$: unknown BCs, $\delta = 0.01$

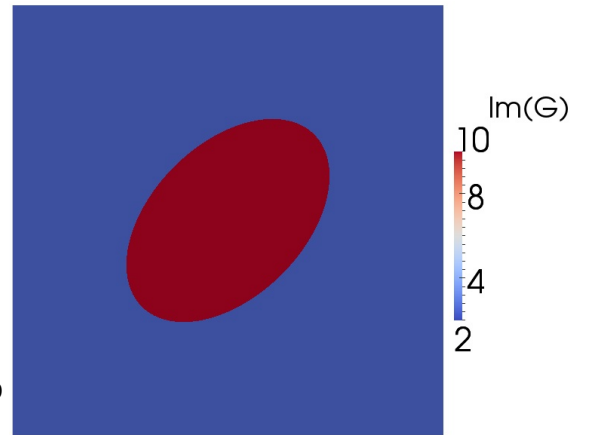


(f) $\text{Re}(G^*)$: unknown BCs, $\delta = 0.05$

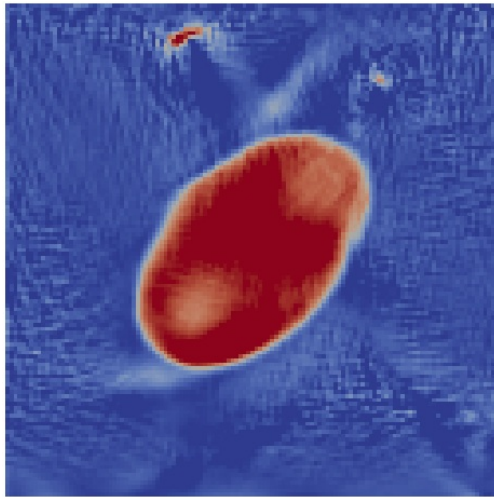
Figure 3: Example 1, reconstruction of $\text{Re}(G)$. Units: kPa, mm



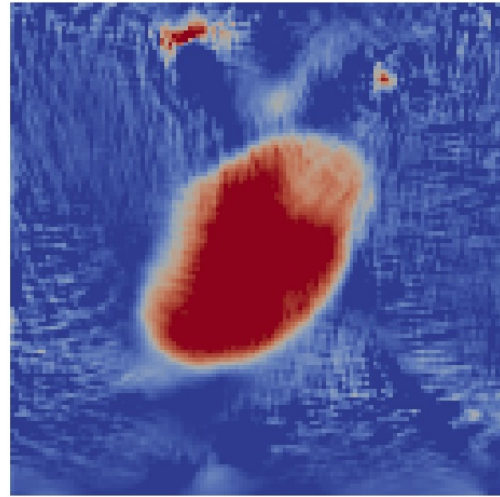
(a) Line plot along AB (see Fig. 1)



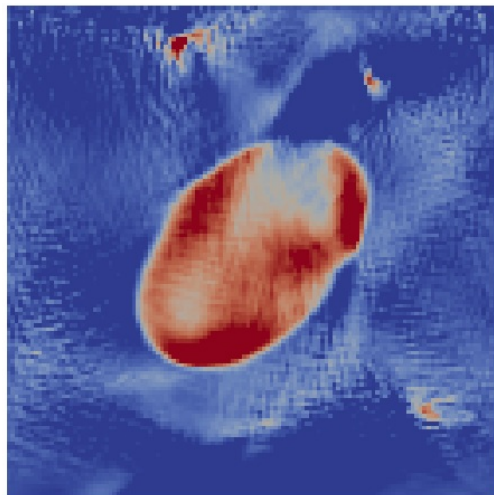
(b) Reference $\text{Im}(G^{\text{ref}})$



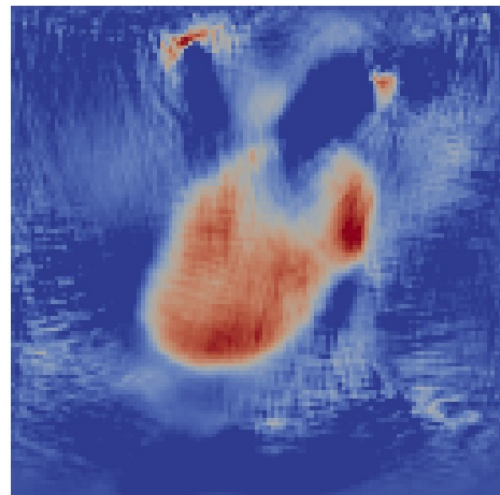
(c) $\text{Im}(G^*)$: known BCs, $\delta = 0.01$



(d) $\text{Im}(G^*)$: known BCs, $\delta = 0.05$



(e) $\text{Im}(G^*)$: unknown BCs, $\delta = 0.01$



(f) $\text{Im}(G^*)$: unknown BCs, $\delta = 0.05$

Figure 4: Example 1, reconstruction of $\text{Im}(G)$. Units: kPa, mm

Table 1 shows the values of the weighting parameter α selected according to Morozov’s principle (see Section 3.5) for the results corresponding to Scenarios 1 and 2, respectively. These tables also report the relative L^1 and L^2 reconstruction errors as defined in (37). For comparison purposes, the inverse problem was also solved using the purely elastic initial guess $(B_{\text{init}}, G_{\text{init}}) = (B_0, \text{Re}(G_0))$; the corresponding values for α and the relative errors in the reconstructed moduli are also reported in Table 1. As it can be appreciated in these tables, the value of α decreased with increasing noise level – which is indeed expected because the noisier the measurement data, the less strictly it should be enforced. Additionally, the α values corresponding to the elastic initial guess are lower by a few orders of magnitude than those corresponding to the viscoelastic initial guess. This is a direct result of the choice of normalization used for this work, which is presented in (34). More specifically, an elastic initial guess yields \mathbf{u}_{init} with a larger magnitude than the one obtained using a viscous initial guess (holding the real part constant), since \mathbf{u}_{init} in the latter case is attenuated by damping. Hence, \mathbf{u}_{init} with a larger magnitude leads to a higher value of A , which is compensated with a lower value for α in order to satisfy Morozov’s principle.

Table 1: Algorithm diagnostics for Example 1.

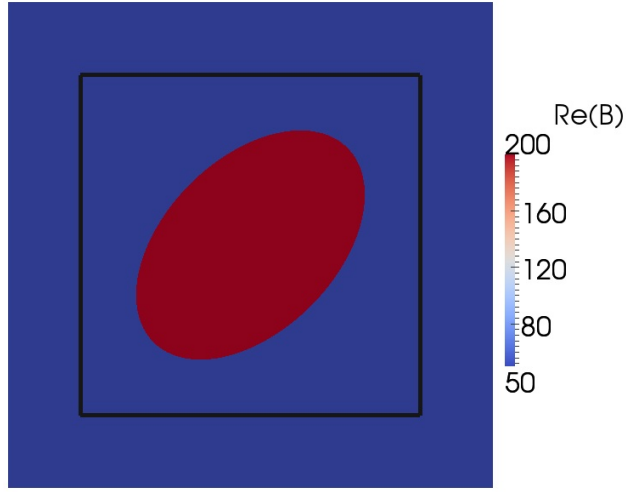
| Scenario | Initial guess | δ | α | $e_1[B]$ | $e_2[B]$ | $e_1[G]$ | $e_2[G]$ |
|-------------|-------------------------|----------|----------------------|----------|----------|----------|----------|
| known BCs | Background | 0.01 | 0.20 | 0.15 | 0.23 | 0.15 | 0.15 |
| | | 0.05 | 0.14 | 0.28 | 0.36 | 0.25 | 0.24 |
| | Real part of background | 0.01 | 6.6×10^{-5} | 0.16 | 0.22 | 0.15 | 0.15 |
| | | 0.05 | 4.9×10^{-5} | 0.27 | 0.33 | 0.26 | 0.25 |
| unknown BCs | Background | 0.01 | 0.30 | 0.29 | 0.30 | 0.32 | 0.29 |
| | | 0.05 | 0.10 | 0.45 | 0.48 | 0.40 | 0.39 |
| | Real part of background | 0.01 | 8.9×10^{-5} | 0.27 | 0.29 | 0.34 | 0.29 |
| | | 0.05 | 2.7×10^{-5} | 0.41 | 0.46 | 0.47 | 0.42 |

It is important to point out that the reconstruction errors presented in Table 1 may provide a misleading sense of the accuracy of the reconstructed moduli. For instance, small errors in the shape or location of the reconstructed inclusion may lead to relatively high L^1 and L^2 errors, which are nevertheless not truly representative of the visual reconstruction quality seen in Figures 2–4. The L^1 and L^2 errors given in Table 1, however, are useful for making relative comparisons between the different reconstructions. For example, reconstruction errors increase as expected with either increasing data noise or loss of boundary information. On the other hand, these errors are rather insensitive to the nature of the initial guess (i.e., elastic vs. viscoelastic), i.e. the MECE-based algorithm exhibits robustness with respect to the initial guess.

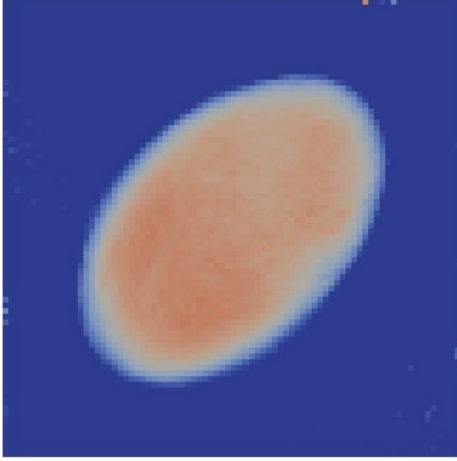
Remark 5. *We also investigated the case in which the sought bulk modulus was also viscoelastic. We consistently observed that both $\text{Re}(B)$ and $\text{Im}(B)$ were reconstructed with less accuracy than $\text{Re}(G)$ and $\text{Im}(G)$. The $\text{Im}(B)$ component showed the largest reconstruction error, to the point that the inclusion was not identified. These results are not shown herein for the sake of brevity. However, we confirmed that the observed inaccuracy in the reconstruction of $\text{Im}(B)$ and $\text{Im}(G)$ stems from the specific geometry and loading configuration used for the examples shown herein. More accurate reconstructions could be obtained using, for instance, multiple experiments in which the loads and boundary conditions are varied.*

4.2. Example 2: 2D reconstruction with window

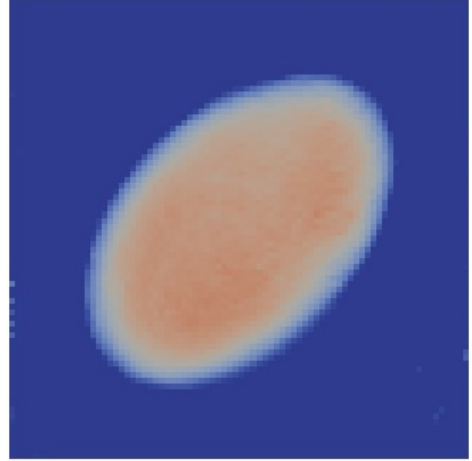
This example aims to highlight the ability of the proposed approach to reconstruct the shear and bulk moduli fields in a subdomain, or window, of the original problem domain Ω and also to further investigate the influence of the initial guess $(B_{\text{init}}, G_{\text{init}})$ on the reconstruction. The problem setup used is identical to that of Example 1 except for the fact that measured displacements are now assumed to be available only in a window $\Omega_w \subset \Omega$, taken as a square subdomain with sides of 28 mm centered at the center of Ω (so that $|\Omega_w| = 0.49|\Omega|$). The MECE-based formulation will be applied to the subdomain Ω_w and in the



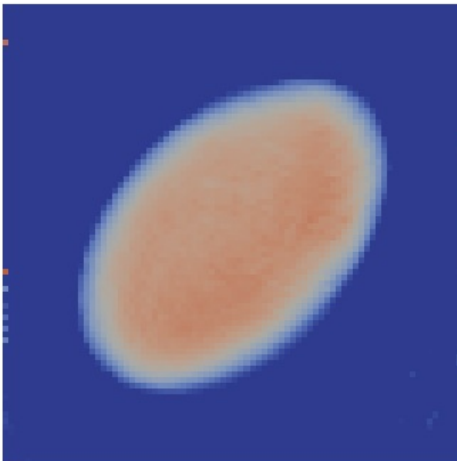
(a) Reference with window



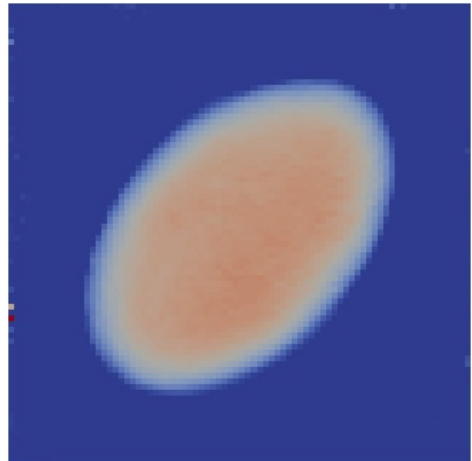
(b) Initial guess 1: real part of background



(c) Initial guess 2: background

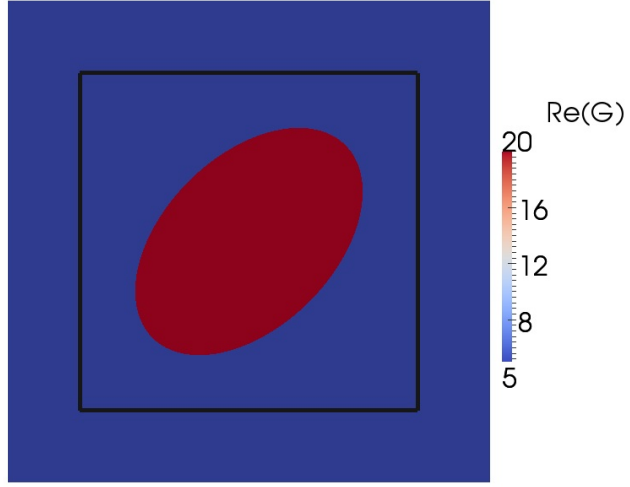


(d) Initial guess 3: $B_{\text{init}} = 50$; $G_{\text{init}} = 5 + 4.5i$

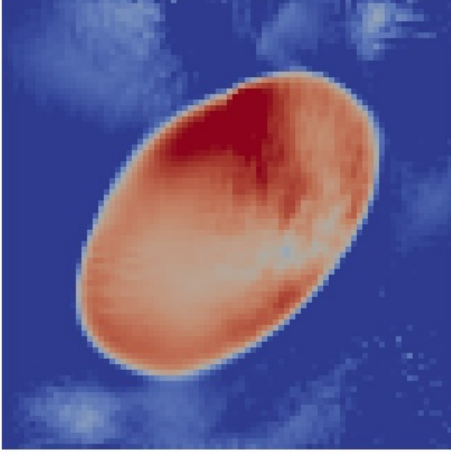


(e) Initial guess 4: $B_{\text{init}} = 50$; $G_{\text{init}} = 10 + 3i$

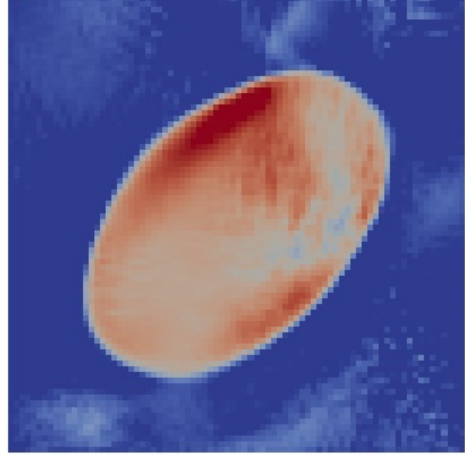
Figure 5: Example 2, reconstruction of $\text{Re}(B)$. Background is $B_0 = 50$ and $G_0 = 5 + 2.5i$. Units: kPa, mm



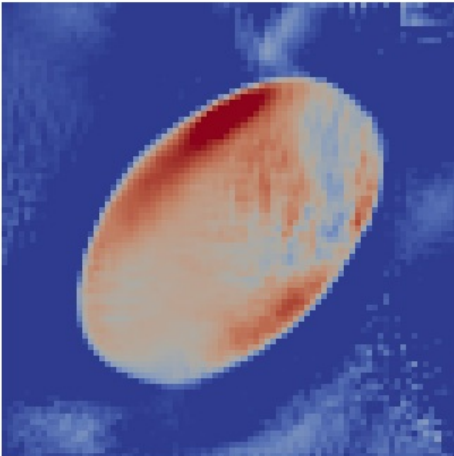
(a) Reference with window



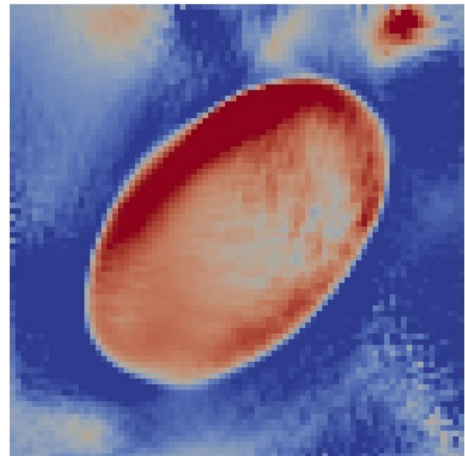
(b) Initial guess 1: real part of background



(c) Initial guess 2: background

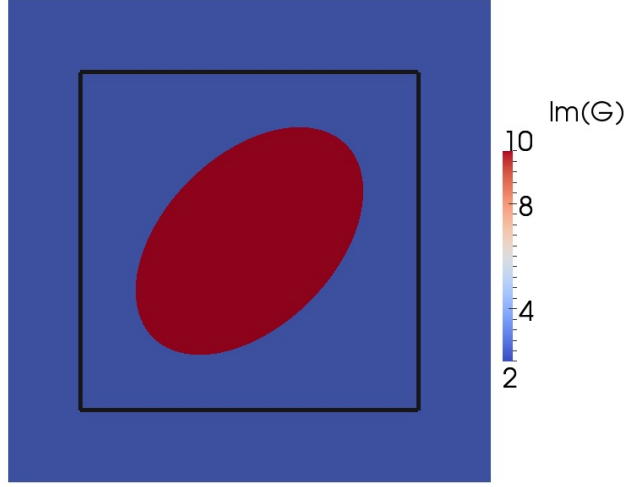


(d) Initial guess 3: $B_{\text{init}} = 50$; $G_{\text{init}} = 5 + 4.5i$

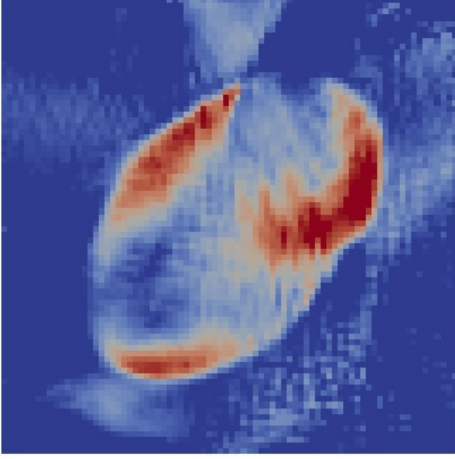


(e) Initial guess 4: $B_{\text{init}} = 50$; $G_{\text{init}} = 10 + 3i$

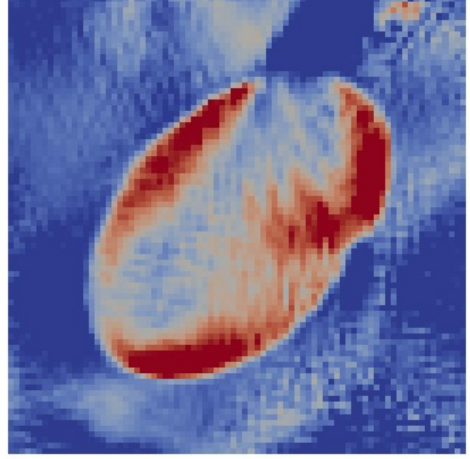
Figure 6: Example 2, reconstruction of $\text{Re}(G)$. Background is $B_0 = 50$ and $G_0 = 5 + 2.5i$. Units: kPa, mm



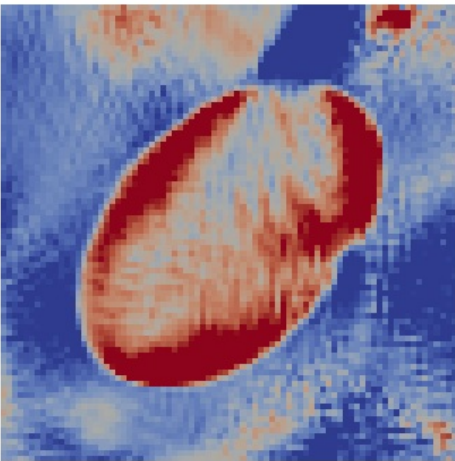
(a) Reference with window



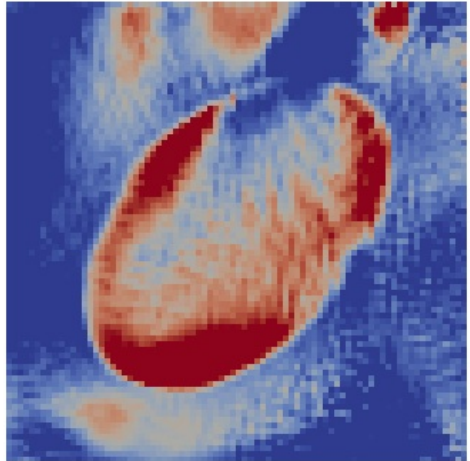
(b) Initial guess 1: real part of background



(c) Initial guess 2: background



(d) Initial guess 3: $B_{\text{init}} = 50$; $G_{\text{init}} = 5 + 4.5i$



(e) Initial guess 4: $B_{\text{init}} = 50$; $G_{\text{init}} = 10 + 3i$

Figure 7: Example 2, reconstruction of $\text{Im}(G)$. Background is $B_0 = 50$ and $G_0 = 5 + 2.5i$. Units: kPa, mm

absence of boundary condition information. A uniform reconstruction mesh is defined on Ω_w featuring 6,400 quadrilateral (Q4) elements. Synthetic data noise is generated using (36) with $\delta = 0.01$. Four different initial guesses are considered, with the bulk modulus set in all cases to $B_{\text{init}} = B_0 = 50$ kPa and the following choices for the shear modulus: 1) $G_{\text{init}} = \text{Re}(G_0) = 5$ kPa (elastic initial guess); 2) $G_{\text{init}} = G_0 = 5 + 2.5i$ kPa; 3) $G_{\text{init}} = 5 + 4.5i$ kPa; and 4) $G_{\text{init}} = 10 + 3i$ kPa. Thus, each initial guess involves a different level of damping in the shear modulus.

Figures 5, 6, and 7 show the reconstructions obtained with different initial guesses for the alternating directions algorithm. As it can be seen in Figure 5, the different initial guesses did not have a significant effect on the reconstruction of $\text{Re}(B)$. This is indeed expected because B_{init} was the same for all cases. Moreover, these reconstructions correctly identified the background value B_0 but underestimated B_1 in the inclusion. This is also seen in Figure 6 to be the case for $\text{Re}(G)$, whose estimated value is nevertheless more accurate. In addition, initial guess 4 resulted in higher reconstruction errors for $\text{Re}(G)$ than the other reconstructions, which seems to be a reflection of the large discrepancy between $\text{Re}(G_{\text{init}})$ and $\text{Re}(G_0)$ for that case. Finally, all reconstructions of $\text{Re}(B)$ and $\text{Re}(G)$ correctly identified the inclusion shape. The reconstruction of $\text{Im}(G)$, shown in Figure 7, is the most affected by the different initial guesses considered. The quality of the reconstruction inside the inclusion locus improves with increasing values of $\text{Im}(G_{\text{init}})$, with initial guess 3 providing the best result. This trend appears to be reversed, however, for the reconstruction in the background region. Additionally, the use of a window led to a degradation in the reconstruction quality. We are currently investigating the exact reason for this degradation.

Table 2 shows the value for α obtained according to Morozov’s principle and the relative L^1 and L^2 reconstruction errors for the different initial guesses considered. The reconstruction errors are seen to not depend significantly on the initial guess, which confirms the robustness of the algorithm in this sense. However, these errors are, in general, slightly greater than their counterparts in Example 1, which is evidence of some degradation in the reconstruction quality when using a window. Moreover, as in Example 1, the value for α is lower for the (elastic) initial guess than for the others, but the drop is not as sharp as in Example 1. We conjecture this is due to the difference in size (i.e., area) between Ω_w and Ω and the way the domain affects α through (34).

Table 2: Example 2: algorithm diagnostics.

| Initial guess | | α | $e_1[B]$ | $e_2[B]$ | $e_1[G]$ | $e_2[G]$ |
|----------------------------|----------------------------------|----------|----------|----------|----------|----------|
| $B_{\text{init}} = 50$ kPa | $G_{\text{init}} = 5$ kPa | 0.05 | 0.55 | 0.45 | 0.53 | 0.41 |
| $B_{\text{init}} = 50$ kPa | $G_{\text{init}} = 5 + 2.5i$ kPa | 0.43 | 0.58 | 0.47 | 0.51 | 0.40 |
| $B_{\text{init}} = 50$ kPa | $G_{\text{init}} = 5 + 4.5i$ kPa | 0.61 | 0.57 | 0.46 | 0.60 | 0.44 |
| $B_{\text{init}} = 50$ kPa | $G_{\text{init}} = 10 + 3i$ kPa | 0.43 | 0.58 | 0.48 | 0.65 | 0.47 |

4.3. Example 3: 3D reconstruction with 3D data

This example is designed to showcase the ability of the MECE-based reconstruction algorithm to scale to more general three-dimensional situations. The reconstructions performed for this example were done for the unknown boundaries scenario and using noisy displacement data. The domain Ω , shown in Figure 8, consists of a cube (edge length: 4 cm). An inclusion, whose support is an elliptic cylinder (length: 2 cm; axis along the z direction; major and minor semiaxes: 11.3 mm and 7 mm, with 45° inclination) whose center coincides with that of the cube, is to be identified.

The frequency used in this example was 50 Hz. The target moduli are $(B_0, G_0) = (100, 20 + 2i)$ kPa for the background and $(B_0, G_0) = (300, 60 + 8i)$ kPa for the inclusion. The boundary conditions used to generate the measurement data consisted of compression and shearing loads on every face of the cube except the bottom face, which was fixed. The data generation mesh involved 60,000 quadratic tetrahedral elements, while the coarser reconstruction mesh used about 15,600 trilinear hexahedral elements. Synthetic data noise is again generated using (36), with $\delta = 0.01$.

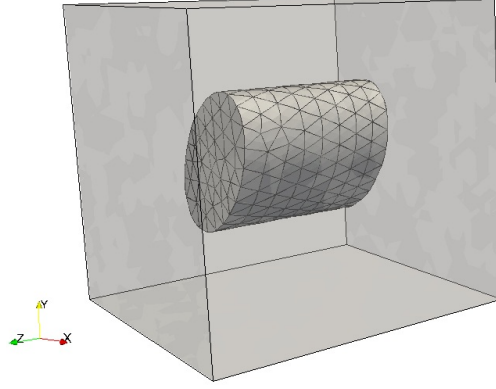
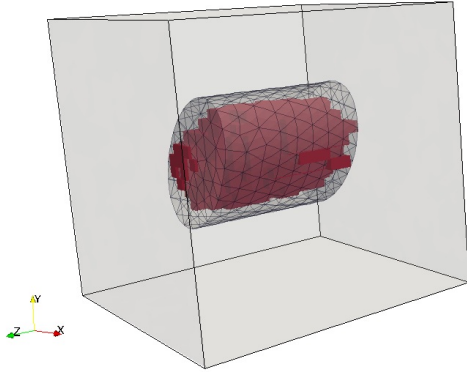
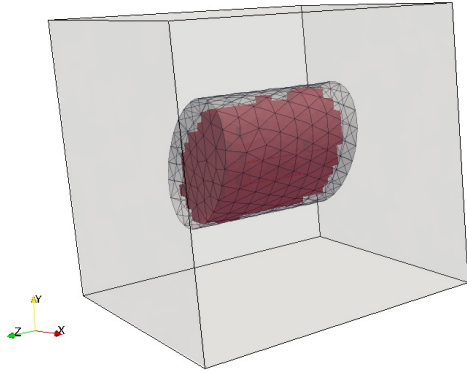


Figure 8: Example 3: domain and inclusion

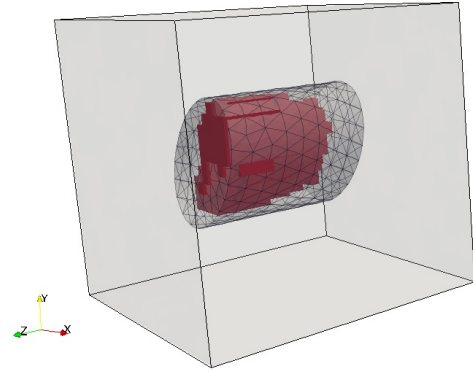
The initial guess for the MECE-based algorithm is set to $(B_{\text{init}}, G_{\text{init}}) = (B_0, G_0)$. Figure 9 shows threshold plots for all reconstructed values of the moduli. These plots show the cube background and the inclusion with corresponding elements from the mesh shaded in for reference purposes. Additionally, Figure 10 shows cuts parallel to the cube faces, going through the center of the domain. The algorithm was able to



(a) $\text{Re}(B)$. $[\text{Min}, \text{Max}] = [175, 234]$



(b) $\text{Re}(G)$. $[\text{Min}, \text{Max}] = [35, 46]$



(c) $\text{Im}(G)$. $[\text{Min}, \text{Max}] = [4.5, 8]$

Figure 9: Example 3: threshold plots. Intervals represent bounds on values of elements shown in red. Units: kPa

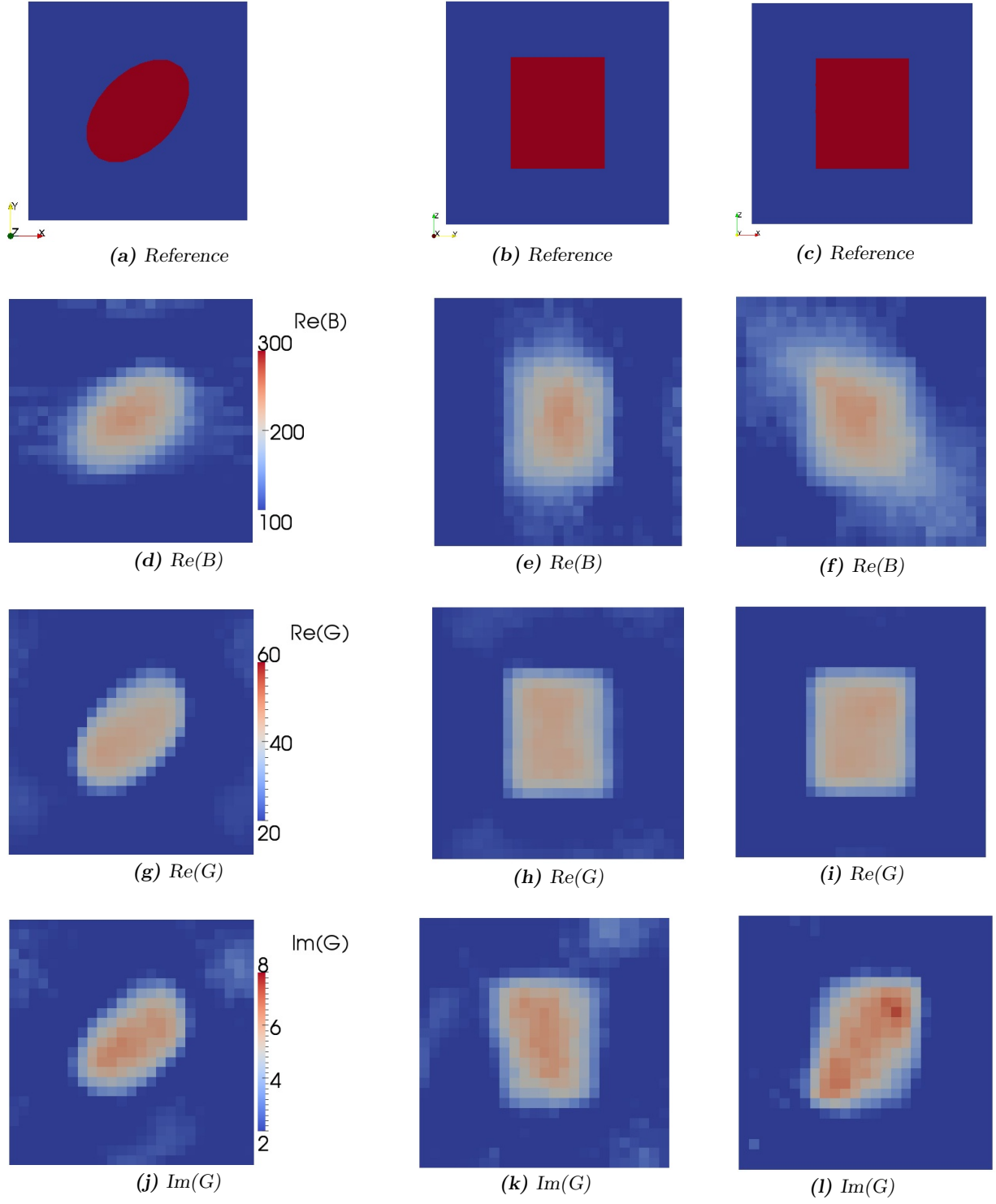


Figure 10: Example 3, reconstructed moduli in planes through center of domain: xy -plane (left column), yz -plane (middle column), xz -plane (right column). Units: kPa

correctly identify the location and shape of the inclusion as well as the value of the background’s moduli. The reconstructed values in the inclusion region, nevertheless, underestimate in all instances the target values. Indeed, the reconstructed maximum value in the domain is less than the corresponding target inclusion modulus in all cases.

Table 3 shows the value of the weighting parameter α , selected according to Morozov’s principle, and the relative reconstruction errors. For comparison purposes, the scenarios where boundary conditions are either unknown or known are both considered. As in all other numerical experiments performed for this investigation, reconstructions obtained without boundary condition information are less accurate than those obtained with known boundary conditions. However, the former reconstructions, as demonstrated by Figures 9 and 10, remain meaningful and useful for biomedical imaging purposes.

Table 3: Example 3: algorithm diagnostics.

| Boundary Conditions | α | $e_1[B]$ | $e_2[B]$ | $e_1[G]$ | $e_2[G]$ |
|---------------------|----------|----------|----------|----------|----------|
| Known | 4.9 | 0.25 | 0.30 | 0.13 | 0.16 |
| Unknown | 2.7 | 0.38 | 0.40 | 0.31 | 0.35 |

5. Conclusions

The intended contributions of this work, devoted to the imaging of linearly viscoelastic heterogeneous moduli using interior data, include (i) the development of an algorithm exploiting a generalized error in constitutive equation functional which handles in a very natural way situations where boundary conditions are not known and (ii) a demonstration of its feasibility on 2D and 3D synthetic imaging problems involving up to tens of thousands of unknown viscoelastic moduli and using incomplete and noisy displacement data without information on the boundary conditions. In addition, the resulting optimality sub-system for the mechanical fields was shown to be invertible. Regularization of the inverse problem of viscoelasticity imaging is achieved using Morozov’s discrepancy principle, which assumes the availability of prior information on the level of data noise. Our proposed approach would be particularly useful in the area of biomechanical imaging, which aims to image the material parameters of a tissue from displacements measured in its interior and where accurate information on boundary conditions is not readily available.

Future directions of investigation include the following: 1) to assess the algorithm against real experimental data; 2) to formulate alternative definitions of the ECE functional based on the Legendre-Fenchel error density which would easily allow multi-frequency data and not involve a normalization tensor \mathcal{P} ; 3) to extend the formulation to address imaging problems in which measured data from multiple experiments is available; 4) to determine the convergence properties of the alternating directions strategy; and 5) to devise regularization techniques to select the weighting parameter α in cases in which the noise level in the data is unknown.

Acknowledgments Wilkins Aquino and Manuel Diaz were partially supported by NIH Grant # R01CA174723.

References

- [1] Aguilo M.A., Aquino W., Brigham J.C., Fatemi M. An inverse problem approach for elasticity imaging through vibroacoustics. *Medical Imaging, IEEE Transactions on*, **29**:1012–1021 (2010).
- [2] Albocher U., Oberai A.A., Barbone P.E., Harari I. Adjoint-weighted equation for inverse problems of incompressible plane-stress elasticity. *Computer Methods in Applied Mechanics and Engineering*, **198**:2412–2420 (2009).
- [3] Allix O., Feissel P., Nguyen H.M. Identification strategy in the presence of corrupted measurements. *Engineering Computations*, **22**:487–504 (2005).
- [4] Banerjee B., Walsh T.F., Aquino W., Bonnet M. Large scale parameter estimation problems in frequency-domain elastodynamics using an error in constitutive equation functional. *Computer Methods in Applied Mechanics and Engineering*, **253**:60 – 72 (2013).

- [5] Barthe D., Ladeveze P., Deraemaeker A., Loch S.L. Validation and updating of industrial models based on the constitutive relation error. *AIAA journal*, **42**:1427–1434 (2004).
- [6] Bonnet M., Constantinescu A. Inverse problems in elasticity. *Inverse problems*, **21**:R1 (2005).
- [7] Brigham J., Aquino W., Mitri F., Greenleaf J., Fatemi M. Inverse estimation of viscoelastic material properties for solids immersed in fluids using vibroacoustic techniques. *Journal of applied physics*, **101**:023509–023509 (2007).
- [8] Christensen R. *Theory of viscoelasticity: an introduction*. Academic press (1982).
- [9] Colton D., Kress R. *Inverse acoustic and electromagnetic scattering theory*, vol. 93. Springer (2012).
- [10] Doyley M., Meaney P., Bamber J. Evaluation of an iterative reconstruction method for quantitative elastography. *Physics in Medicine and Biology*, **45**:1521 (2000).
- [11] Feissel P., Allix O. Modified constitutive relation error identification strategy for transient dynamics with corrupted data: The elastic case. *Computer methods in applied mechanics and engineering*, **196**:1968–1983 (2007).
- [12] Fung Y. *Biomechanics: mechanical properties of living tissues*. Biomechanics / Y. C. Fung. Springer-Verlag (1981).
- [13] Gao L., Parker K., Lerner R., Levinson S. Imaging of the elastic properties of tissue—A review. *Ultrasound in medicine & biology*, **22**:959–977 (1996).
- [14] Grasely Z. *Measuring and modeling the time-dependent response of cementitious materials to internal stresses*. Ph.D. thesis, University of Illinois at Urbana-Champaign (2006).
- [15] Greenleaf J.F., Fatemi M., Insana M. Selected methods for imaging elastic properties of biological tissues. *Annual review of biomedical engineering*, **5**:57–78 (2003).
- [16] Isakov V. *Inverse problems for partial differential equations*, vol. 127. Springer (2006).
- [17] Ladevèze P., Leguillon D. Error estimate procedure in the finite element method and applications. *SIAM Journal on Numerical Analysis*, **20**:485–509 (1983).
- [18] Ladevèze P., Nedjar D., Reynier M. Updating of finite element models using vibration tests. *AIAA journal*, **32**:1485–1491 (1994).
- [19] Nocedal J., Wright S.J. *Numerical Optimization 2nd*. Springer (2006).
- [20] Oberai A.A., Gokhale N.H., Feijoo G.R. Solution of inverse problems in elasticity imaging using the adjoint method. *Inverse Problems*, **19**:297 (2003).
- [21] Oliphant T.E., Manduca A., Ehman R.L., Greenleaf J.F. Complex-valued stiffness reconstruction for magnetic resonance elastography by algebraic inversion of the differential equation. *Magnetic resonance in Medicine*, **45**:299–310 (2001).
- [22] Ophir J., Alam S., Garra B., Kallel F., Konofagou E., Krouskop T., Varghese T. Elastography: ultrasonic estimation and imaging of the elastic properties of tissues. *Proceedings of the Institution of Mechanical Engineers, Part H: Journal of Engineering in Medicine*, **213**:203–233 (1999).
- [23] Park E., Maniatty A.M. Shear modulus reconstruction in dynamic elastography: time harmonic case. *Physics in medicine and biology*, **51**:3697 (2006).
- [24] Parker K., Gao L., Lerner R., Levinson S. Techniques for elastic imaging: a review. *Engineering in Medicine and Biology Magazine, IEEE*, **15**:52–59 (1996).
- [25] Parker K.J., Taylor L.S., Gracewski S., Rubens D.J. A unified view of imaging the elastic properties of tissue. *The Journal of the Acoustical Society of America*, **117**:2705 (2005).
- [26] Schenk O., Gärtner K. Solving unsymmetric sparse systems of linear equations with PARDISO. *Future Generation Computer Systems*, **20**:475–487 (2004).
- [27] Schenk O., Gärtner K. On fast factorization pivoting methods for sparse symmetric indefinite systems. *Electronic Transactions on Numerical Analysis*, **23**:158–179 (2006).
- [28] Sinkus R., Tanter M., Catheline S., Lorenzen J., Kuhl C., Sondermann E., Fink M. Imaging anisotropic and viscous properties of breast tissue by magnetic resonance-elastography. *Magnetic resonance in medicine*, **53**:372–387 (2005).
- [29] Warner J.E., Diaz M.I., Aquino W., Bonnet M. Inverse material identification in coupled acoustic-structure interaction using a modified error in constitutive equation functional. *Computational Mechanics*, **54**:1–15 (2014).
- [30] Zhang Y., Oberai A.A., Barbone P.E., Harari I. Solution of the time-harmonic viscoelastic inverse problem with interior data in two dimensions. *International Journal for Numerical Methods in Engineering*, **92**:1100–1116 (2012).